Title

How Pt Influences H2 Reactions on High Surface-Area Pt/CeO2 Powder Catalyst Surfaces

Journal

JACS Au, 3(8)

ISSN

2691-3704

Authors

Lee, Jaeha

Tieu, Peter

Finzel, Jordan

et al.

Publication Date

2023-08-28

DOI

10.1021/jacsau.3c00330

JACS Au
AN OPEN ACCESS JOURNAL OF THE AMERICAN CHEMICAL SOCIETY

pubs.acs.org/jacsau
Article

How Pt Influences H_2 Reactions on High Surface-Area Pt/CeO_2 Powder Catalyst Surfaces

Jaeha Lee,[#] Peter Tieu,[#] Jordan Finzel, Wenjie Zang, Xingxu Yan, George Graham, Xiaoqing Pan,* and Phillip Christopher*

Cite This: *JACS Au* 2023, 3, 2299−2313
Read Online
ACCESS | Metrics & More | Article Recommendations | Supporting Information

ABSTRACT: The addition of platinum-group metals (PGMs, e.g., Pt) to CeO_2 is used in heterogeneous catalysis to promote the rate of redox surface reactions. Well-defined model system studies have shown that PGMs facilitate H_2 dissociation, H-spillover onto CeO_2 surfaces, and CeO_2 surface reduction. However, it remains unclear how the heterogeneous structures and interfaces that exist on powder catalysts influence the mechanistic picture of PGM-promoted H_2 reactions on CeO_2 surfaces developed from model system studies. Here, controlled catalyst synthesis, temperature-programmed reduction (TPR), in situ infrared spectroscopy (IR), and in situ electron energy loss spectroscopy (EELS) were used to interrogate the mechanisms of how Pt nanoclusters and single atoms influence H_2 reactions on high-surface area Pt/CeO_2 powder catalysts. TPR showed that Pt promotes H_2 consumption rates on Pt/CeO_2 even when Pt exists on a small fraction of CeO_2 particles, suggesting that H-spillover proceeds far from Pt−CeO_2 interfaces and across CeO_2−CeO_2 particle interfaces. IR and EELS measurements provided evidence that Pt changes the mechanism of H_2 activation and the rate limiting step for Ce^{3+}, oxygen vacancy, and water formation as compared to pure CeO_2. As a result, higher-saturation surface hydroxyl coverages can be achieved on Pt/CeO_2 compared to pure CeO_2. Further, Ce^{3+} formed by spillover-H from Pt is heterogeneously distributed and localized at and around interparticle CeO_2−CeO_2 boundaries, while activated H_2 on pure CeO_2 results in homogeneously distributed Ce^{3+}. Ce^{3+} localization at and around CeO_2−CeO_2 boundaries for Pt/CeO_2 is accompanied by surface reconstruction that enables faster rates of H_2 consumption. This study reconciles the materials gap between model structures and powder catalysts for H_2 reactions with Pt/CeO_2 and highlights how the spatial heterogeneity of powder catalysts dictates the influence of Pt on H_2 reactions at CeO_2 surfaces.

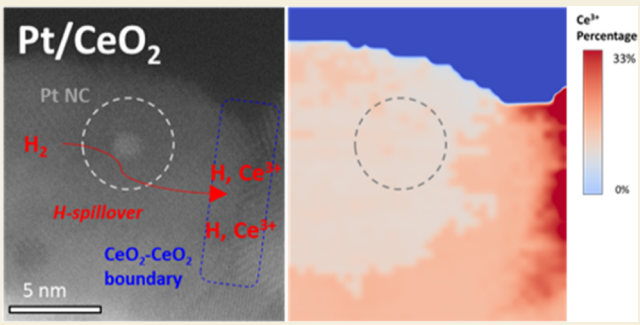

KEYWORDS: *platinum, ceria, catalysts, redox reactions, materials gap, spillover*

INTRODUCTION

CeO_2 has been intensively studied as a catalyst for various heterogeneous catalytic reactions and as a support for platinum-group metals (PGMs).[1] For example, dissociated H_2 on CeO_2 can participate in selective hydrogenation or dehydrogenation reactions.[2−4] In addition, dissociated H_2 can induce the reduction of Ce^{4+} to Ce^{3+} and the formation of oxygen vacancies (V_o) through H_2O formation and desorption, which can facilitate the adsorption and activation of various reactants (e.g., CO_2 and H_2O).[5−8] Therefore, understanding the H_2 activation mechanism on CeO_2 and the resulting influence on CeO_2 surface chemistry is critical for understanding various catalytic processes.

Surface science analyses have shown that PGMs promote interactions between H_2 and CeO_2 surfaces by dissociating H_2 and spilling over H to CeO_2.[9−13] However, the translation of this mechanistic picture to high-surface area powder catalysts is complicated by spatial heterogeneities, such as PGMs existing as single atoms (SAs) or nanoclusters (NCs), and the existence of CeO_2−CeO_2 particle boundaries, which may affect interactions with H_2. In addition, most reports assert that V_o (and associated Ce^{3+}) species produced via H_2 interactions with PGM/CeO_2 localize around PGMs.[6,14−18] However, the influence of Pt on various elementary steps involved in V_o formation across the CeO_2 surface has not been resolved, and direct measurements of Ce^{3+} spatial distribution in nonmodel PGM-supported CeO_2 samples are lacking. Thus, while it is appreciated that H-spillover from PGMs influences CeO_2 surface chemistry, information is lacking for powder catalysts, particularly the mechanism of PGM-promoted CeO_2 surface reduction, the influence of heterogeneity on the PGM

Received: June 22, 2023
Revised: July 12, 2023
Accepted: July 13, 2023
Published: August 8, 2023

structure and CeO_2−CeO_2 interparticle interactions, and the resulting Ce^{3+} spatial distribution.

To address these missing mechanistic insights, we prepared a series of high-surface area, powdered Pt/CeO_2 materials with varying Pt structures (SAs or NCs), Pt weight loading (0.0005−2 wt %), and dilutions with pure CeO_2 to isolate the role of the Pt structure, Pt−CeO_2 contacts, and CeO_2−CeO_2 interactions in H_2 reactions with CeO_2 surfaces. In situ spectroscopy and microscopy coupled to measurements of H_2 consumption rates provide sample-averaged and spatially resolved information about the kinetics, mechanisms, and locations of H-spillover and Ce^{3+} formation. Experimental evidence suggests that while H_2 dissociates heterolytically on pure CeO_2 surfaces, Pt promotes homolytic H_2 dissociation and subsequent H-spillover onto CeO_2 surfaces, resulting in more than a twofold increase in saturation hydroxyl coverage compared to pure CeO_2. Samples containing predominantly Pt NCs exhibit faster rates of homolytic H_2 dissociation than samples containing predominantly Pt SAs, and further, H-spillover can occur through contact between CeO_2 particles even when a significant fraction of CeO_2 particles do not contain Pt. Time-resolved IR spectroscopy of H_2 reactions under isothermal conditions suggests that the conversion of heterolytic H_2 dissociation products into homolytic products is the rate-limiting step for H_2O evolution on pure CeO_2, but Pt-mediated homolytic H_2 dissociation and H-spillover remove this kinetic limitation and promote the rate of H_2O evolution from CeO_2 even far from the Pt−CeO_2 interface. In addition, while Ce^{3+} formation on pure CeO_2 surfaces occurs homogeneously across the surface, Pt-containing samples exhibit increased hydroxyl coverages on CeO_2 and localization of Ce^{3+} at and around the boundaries between CeO_2 particles rather than around Pt. The high hydroxyl coverage on CeO_2 caused by H-spillover from Pt induces irreversible changes to interparticle CeO_2 interfaces resulting in the oriented attachment of neighboring CeO_2 particles. The reconstructed CeO_2 surfaces at the boundaries between aligned CeO_2 particles appear to serve as highly reactive sites for H_2 consumption. This study provides mechanistic insights into the influence of spatial heterogeneities in powdered Pt/CeO_2 samples on their H_2 activation and CeO_2 surface reduction reactivity.

EXPERIMENTAL SECTION

Materials

High-purity (99.995%) tetraammineplatinum(II) nitrate (TAPN) purchased from Sigma-Aldrich was used as the Pt precursor. High-surface area CeO_2 was purchased from US Research Nanomaterials and used as the support in this study. The BET surface area of CeO_2 oxidized at 500 °C with 20% O_2/He for 2 h was estimated to be 68 m^2/g from N_2 adsorption/desorption measurements. 28−39% concentration NH_4OH solution was purchased from Sigma-Aldrich and used in catalyst synthesis. γ-Al_2O_3 nanoparticles with an average diameter of 5 nm was purchased from US Research Nanomaterials. 10% H_2/Ar, pure H_2, Ar, 10% O_2/He, and 10% CO/He from Airgas were used in this study.

Catalyst Synthesis

Pt was dispersed on CeO_2 using a modified strong electrostatic adsorption method.[19,20] Pt/CeO_2 samples were prepared at a range of Pt weight loadings from 0.0005 to 2 wt %. Briefly, 0.5 g of CeO_2 was dispersed in 50 mL of deionized H_2O, and the pH of the solution was adjusted to 9.0 using NH_4OH. The point of zero charge of CeO_2 was measured to be 3.4. Therefore, the CeO_2 surface is deprotonated at a pH of 9.0. Performing syntheses at a pH of 9.0 maximizes Pt dispersion through electrostatic interaction with $[Pt(NH_3)_4]^{2+}$ complexes. Separately, the desired amount of TAPN was dissolved in deionized H_2O and the solution was brought to a pH of 9.0. The TAPN solution was slowly injected into the CeO_2 solution over 12.5 h, and the final mixed solution was heated to 70 °C until dry. The dried Pt/CeO_2 samples were calcined in a tube furnace at 450 °C for 4 h by flowing dry air after ramping up the temperature at a rate of 10 °C/min. The Pt-free CeO_2 was oxidized at 500 °C for 2 h by flowing dry air (ramp rate, 10 °C/min). Note also that the wetting of CeO_2 with the deionized H_2O at a pH of 9.0 did not change the surface reducibility of CeO_2. Pt/CeO_2 was also physically mixed with CeO_2 in different mass ratios (1:19, 1:49, and 1:99) using a vibratory mixer.

H_2-Temperature-Programmed Reduction

H_2-temperature-programmed reduction (H_2-TPR) curves were obtained with 0.03 g of the sample using an Autochem II (Micromeritics) equipped with a thermal conductivity detector (TCD). Typically, samples were oxidized with 10% O_2/He at 400 °C for 1 h to remove impurities, cooled to 50 °C under O_2, and purged with Ar at 50 °C for 30 min and stabilized under 10% H_2/Ar at 50 °C for 1 h, and then the temperature was increased in a linear course to collect H_2-TPR curves. The influence of prereduction on the TPR behavior of pure CeO_2 was assessed by collecting H_2-TPR curves after reduction with 10% H_2/Ar at 450 °C for 1 h followed by re-oxidation with 10% O_2/He at 100 °C for 1 h. Similarly, the influence of prereduction on the TPR behavior of Pt/CeO_2 was studied by collecting H_2-TPR curves after reduction with 10% H_2/Ar at 350 °C for 1 h followed by re-oxidation with 10% O_2/He at 350 °C for 1 h. To confirm that the change in the oxidation state of Pt was not the only cause for the improved H_2 consumption rate following prereduction, Pt(2)/CeO_2 was ex situ reduced with 10% H_2/Ar at 400 °C for 1 h, diluted with pure CeO_2, and then re-oxidized in situ with 10% O_2/He at 350 °C for 1 h. The amount of H_2 consumed during the TPR runs was estimated by integrating the TCD signals.

Fourier-Transform Infrared Spectroscopy

Fourier-transform infrared (FTIR) spectroscopy experiments were carried out in a diffuse reflectance reaction chamber (Harrick Scientific) equipped with ZnSe windows, mounted inside a Praying Mantis diffuse reflectance adapter (Harrick Scientific), and coupled to a Thermo Scientific Nicolet iS10 FTIR spectrometer with a liquid nitrogen-cooled HgCdTe (MCT) detector. The FTIR and Praying Mantis diffuse reflection accessories were purged with dry N_2 during experiments. In a typical experiment, the reactor was loaded with ∼80 mg of 50 nm-sized γ-Al_2O_3 (Sigma-Aldrich), followed by 15 mg of the sample on top of the inert alumina. All spectra are reported in absorbance units.

For the H_2-FTIR experiments, samples were first oxidized with 10% O_2/He at a desired temperature for 30 min, purged with Ar at the same temperature for 30 min, and then reduced with 10% H_2/Ar. Spectra were collected on 1 min time scales. As discussed in the Supporting Information, the IR intensity is sensitive to the "peak to peak" intensity in the interferogram, which is related to the total amount of reflected photons from the sample surface. In addition, the "peak to peak" intensity is sensitive to the temperature or sample color that changes during reduction. Therefore, we maintained the "peak to peak" intensity at 5.0 by focusing/defocusing the lenses. The maximum intensities of the vibrational frequency of surface hydroxyls and the forbidden $^2F_{5/2}$-to-$^2F_{7/2}$ electronic transition of Ce^{3+} were used to compare the rate of formation of these two species. For high-pressure experiments, pure H_2 was used, and the pressure was increased using a back-pressure regulator.

For CO-FTIR experiments, samples were oxidized with 10% O_2/He at 300 °C for 30 min, cooled to 25 °C under O_2, and purged with Ar at 50 °C for 30 min before collecting background spectra. 10% CO/Ar was introduced to the sample at 25 °C for 10 min, and the sample was purged by Ar flow for 2 min to remove the gas-phase CO signal in the IR spectra. The flow rate was maintained at 50 mL/min in all conditions.

https://doi.org/10.1021/jacsau.3c00330
JACS Au 2023, 3, 2299−2313

CO Oxidation Reactivity Measurement

The reactivity of the Pt(0.01)/CeO_2 and "Pt(1)/CeO_2:CeO_2 = 1:99" catalysts in CO oxidation was investigated in a tubular packed-bed reactor. 0.015 g of each sample was diluted with 0.3 g of acid-purified SiO_2 gel. Three different pretreatment protocols were used in this study. (i) To study the catalytic reactivity of the oxidized surfaces, samples were oxidized at 400 °C with 10% O_2/He for 1 h. After cooling to 50 °C under O_2, 1% of CO and 10% of O_2 were introduced for reactivity analysis. (ii) To study the catalytic reactivity of the reduced surfaces, samples were reduced with 10% H_2/Ar at 400 °C for 1 h. After cooling to 50 °C under H_2, samples were purged with Ar for another hour. 1% CO and 10% O_2 were then introduced for reactivity tests. (iii) To study the catalytic reactivity of the re-oxidized surfaces, samples were reduced with 10% H_2/Ar at 400 °C for 1 h, purged with Ar at 400 °C for 1 h, and then re-oxidized with 10% O_2/He at 400 °C for 1 h. After cooling to 50 °C under O_2, 1% CO and 10% O_2 were introduced. After introduction of O_2 and CO to all samples, the temperature was increased from 50 to 400 °C at a ramp rate of 2 °C/min to measure the CO oxidation reactivity of Pt/CeO_2 catalysts. In this study, a CO conversion of less than 10% was used to calculated the turnover frequency, and all Pt was assumed to be accessible to the reactants. The Arrhenius equation was used to estimate E_a. An FTIR spectrometer (Nicolet 6700, Thermo Fisher Scientific) with a 2 m gas cell maintained at 120 °C was used to measure the CO concentration. Spectra were recorded using an MCT detector (16 scans, resolution of 1 cm^{-1}).

X-ray Powder Diffraction

X-ray powder diffraction (XRD) patterns were obtained at a voltage of 40 kV and a current of 30 mA with Cu Kα radiation (λ = 0.1542 nm) using a Mode 1 Smartlab diffractometer (Rigaku, Japan). A scanning-step size of 0.02° at a speed of 2.5°/min was used. The Scherrer equation was used to estimate grain sizes.

Surface Area Measurement

N_2 adsorption/desorption isotherms were measured on a Micromeritics 3Flex Porosimeter at liquid N_2 temperature. Before analysis, all samples were degassed at 300 °C for 2 h in vacuum. The Brunauer–Emmett–Teller (BET) method was applied to the N_2 adsorption isotherm to extract surface area estimates.

X-ray Absorption near Edge Structure Spectroscopy

X-ray absorption spectroscopy (XAS) measurements were completed at beamline 9–3 at the Stanford Synchrotron Radiation Lightsource (SSRL) at SLAC National Laboratory. A Si(220) double-crystal monochromator with a 20% detune was used to scan the Pt L_3 absorption edge (11,564 eV). 30 mg of the Pt/CeO_2 catalyst samples (pressed and sieved, 80–120 mesh) were loaded into a 3 mm quartz capillary tube between quartz wool plugs. The capillary was mounted in an in situ XAS reactor cell.[21] Process gasses were supplied via mass flow controllers (Brooks Instrument). The sample was heated via resistive heaters placed above and below the capillary with PID temperature control and a thermocouple placed in contact with the quartz wool of the sample bed. The sample was placed at a 45° angle relative to the beam path, and fluorescence data were collected with a Canberra 100-element Ge detector orthogonal (90°) to the beam path with a 6 absorption length Zn filter and lead shielding to minimize contributions from the scattering of beamline optics. Kapton tape was used to split the initial monochromated beam, and all spectra were calibrated with respect to a Pt reference foil mounted off-axis with a transmission signal collected using a photodiode. Platinum(II) acetylacetonate [$Pt(acac)_2$] and PtO_2 were used as the Pt^{+2} and Pt^{+4} standards, respectively. Reference compounds were pressed into self-supporting pellets with a diameter of 7 mm, and X-ray absorption near edge structure (XANES) scans were collected under ambient conditions.

In situ XANES TPR measurements were used to track the reduction of Pt in Pt/CeO_2 catalysts. Samples were initially oxidized in 20 sccm of 20% O_2/He at 300 °C (heated at 10 °C/min) for 30 min and cooled to 20 °C. XANES scans of the initial oxidized sample were acquired while purging the sample with He (20 sccm). The sample was then exposed to 10% H_2/He (20 sccm), and a TPR was performed up to 400 °C at a ramp rate of 3 °C/min. XANES scans were acquired throughout the TPR.

Transmission Electron Microscopy

High-angle annular dark-field scanning transmission electron microscopy (HAADF-STEM) images were acquired using a JEOL JEM300CF equipped with double aberration correction. In the scanning transmission electron microscopy (STEM) mode, a 32 mrad convergence semi-angle was used, and the dark-field annular detector acquires a signal from 53 to 180 mrad. Powder samples were dispersed in ethanol and dropcast onto the Protochips (North Carolina, USA) E-chips. Pre and post in situ imaging was performed on a Protochips Inspection holder. In situ experiments were performed with a Protochips Atmosphere 210 gas cell system with a gas flow rate of 0.1 cm^3/s at 200 Torr. Pure Ar, 5% H_2/Ar, and 20% O_2/Ar from Airgas were used for the experiments. Prior to imaging, the environment in the holder was pump-purged five times at 200 °C to remove residual atmospheric O and C. For the sequential reduction-oxidation-reduction, the gas cell was exposed to H_2 for 1 h before pump-purging the cell five times with Ar and changing the gas to O_2 for 1 h and finally changing the gas back to H_2 with a pump-purge process. During the pump-purge, the electron beam is turned off to minimize beam exposure.

Electron Energy Loss Spectroscopy

EEL spectra were collected using a Gatan K2 direct electron detector with an energy dispersion of 0.250 eV/channel. Spectra were calibrated to the N K edge. 50 × 50 pixel maps with 0.1 s dwell time were used to generate the EELS mapping images. 10 × 10 pixel maps with 0.05 s dwell time were used to measure the Ce oxidation state at the particle boundary in Figure 5c. Principal component analysis (PCA) was used to improve the signal-to-noise ratio before a power law background subtraction is applied. A double arctan background was applied, and the peaks were fitted with a Voigt peak and then the Ce M_5 and M_4 peak heights were measured. The M_5/M_4 ratio was calculated for each pixel to generate the EELS mapping images with a Gaussian blur applied with sigma = [5,5]. Pixels for the Ce EELS map were selected to match the corresponding HAADF-STEM image by applying a threshold for the Ce signal where below said threshold, the M_5/M_4 ratio was set to zero. Custom Python code was used for PCA, double arctan background subtraction, Voigt peak fitting, and M_5/M_4 ratio measurements to estimate the oxidation state of Ce without bias. The code used in this study is available upon request.

RESULTS AND DISCUSSION

Effect of Pt Amount and Structure and CeO_2 Particle Boundaries on the Rate and Amount of H_2 Consumption

To understand the influence of the Pt structure, Pt–CeO_2 interfaces, and CeO_2–CeO_2 particle interfaces on H_2 surface reactions, a series of materials were prepared that traverse each of these variables. Pt was deposited onto CeO_2 nanoparticles (8.5 nm average diameter estimated from XRD, Figure S1a; 68 m^2/g) via electrostatic adsorption of $Pt(NH_3)_4(NO_3)_3$ from aqueous solutions, followed by calcination in air at 450 °C for 4 h with Pt weight loadings (wt %) ranging from X = 0.0005 to 2 wt % Pt, denoted as Pt(X)/CeO_2. The average number of Pt atoms per CeO_2 particle is 1.0 at ∼0.01 wt % Pt (Figures 1a and S1b), and Pt is primarily atomically dispersed at ≤0.05 wt % Pt, as evidenced by in situ CO-FTIR spectra (Figure S2) and CO oxidation kinetic measurements (Figure S3), whereas Pt exists primarily as Pt_xO_y clusters at a Pt loading of ≥1 wt % for the calcined samples (see Figures S2 and S3 and Supporting Information Discussion I).[20] Mixtures of Pt(1)/CeO_2 with pure CeO_2 were also prepared at mass ratios up to 1:99 [Pt(1)/CeO_2:CeO_2] (Figure 1b) to introduce inter-

https://doi.org/10.1021/jacsau.3c00330
JACS Au 2023, 3, 2299–2313

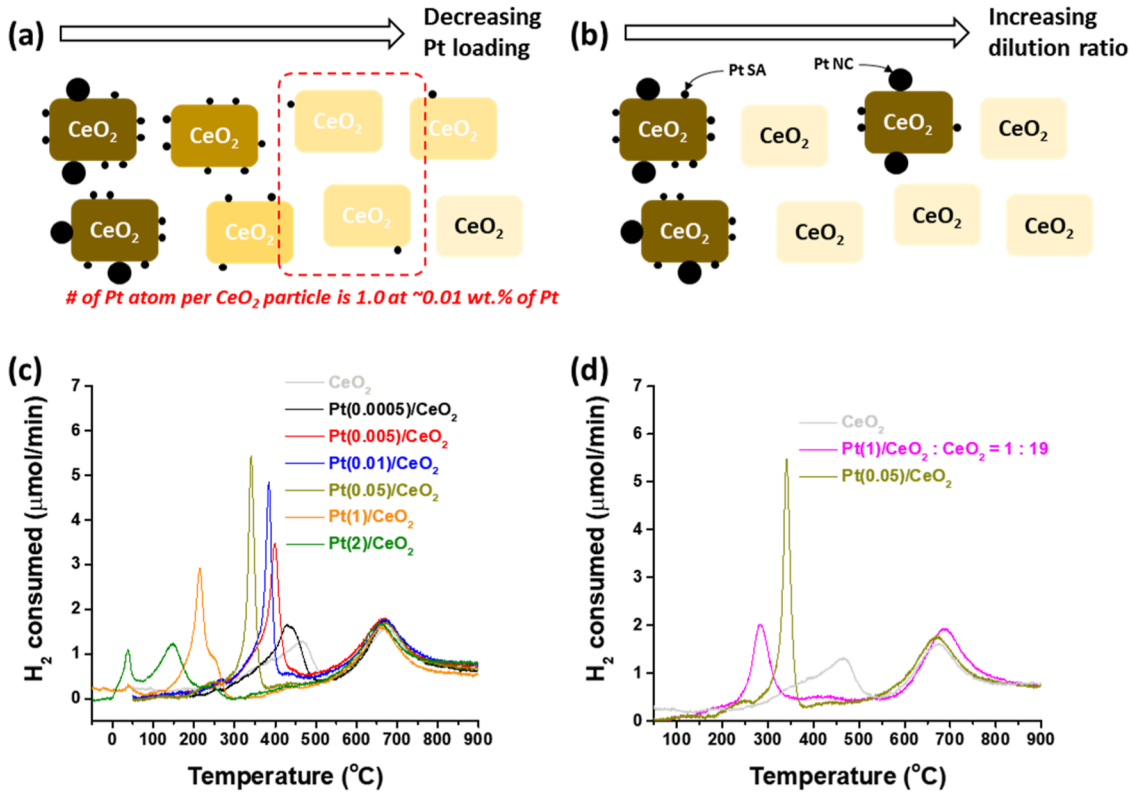

Figure 1. Schematics of Pt/CeO_2 with decreasing Pt loading either by decreasing Pt loading (a) or through dilution with pure CeO_2 (b). The number of Pt atoms per CeO_2 particle becomes 1.0 at ∼0.01 wt % of Pt. (c) H_2-TPR curves of CeO_2 and Pt/CeO_2 with different Pt loadings (ramp rate, 10 °C/min; 10% H_2 at 1 atm). (d) H_2-TPR curves of $Pt(0.05)/CeO_2$ and "$Pt(1)/CeO_2$:CeO_2 = 1:19", which have the same nominal Pt loading but different Pt structures (ramp rate, 10 °C/min; 10% H_2 at 1 atm).

particle CeO_2 contacts and spatially separate Pt from CeO_2 domains.[22]

H_2-TPR was used to probe reactions of H_2 on Pt/CeO_2. H_2-TPR is often used to assess the reducibility (e.g., V_o formation) of oxide surfaces.[23−25] However, H_2-TPR only directly assesses the rate of H_2 consumption during a temperature increase. H_2 consumption can occur due to surface hydroxyl or hydride formation via H_2 dissociation and does not require simultaneous V_o formation. Figure 1c shows the H_2 consumption rates on CeO_2 and Pt/CeO_2 with different Pt loadings collected at a temperature ramp rate of 10 °C/min and using a 10% H_2 feed at atmospheric pressure. H_2 is consumed below 500 °C through reactions with CeO_2 (or Pt/CeO_2) surfaces, while H_2 consumed above 500 °C is due to H_2 reactions with the CeO_2 bulk.[23] TPR measurements were made at <1% H_2 conversion and were devoid of mass transport limitations (Figure S4). Thus, H_2 concentration is effectively constant throughout the catalyst bed, although the Pt/CeO_2 surface structure and composition change during the temperature increase.

Figure 1c shows that the temperature where the peak rate of H_2 consumption occurs due to surface reactions (T_m) increases as the Pt loading decreases from 2 to 0.0005 wt %, while the consumption of H_2 related to reactions with the CeO_2 bulk is not affected. T_m is lower for samples containing <1 Pt atom/CeO_2 particle weight loadings (<0.01 wt %) compared to pure CeO_2. This demonstrates that H_2 dissociation on Pt sites and diffusion of dissociated H across interparticle CeO_2−CeO_2 boundaries occur at faster rates than H_2 dissociation on Pt-free CeO_2 surfaces. H_2 consumption by CeO_2 surface reduction was indistinguishable from H_2 consumed to reduce Pt oxide in Pt/CeO_2 samples when Pt loading ≤1 wt % (Figure 1c), even for H_2-TPR collected at a ramp rate of 3 °C/min (Figure S5). This is likely due to the rapid H-spillover from reduced Pt to CeO_2, linking the reduction of Pt oxide and the H_2 consumption on CeO_2 surfaces.[13,26] However, the H_2 consumption peak centered at 40 °C was observed for $Pt(2)/CeO_2$ (Figure 1c), and a small feature was also observed at a similar temperature for $Pt(1)/CeO_2$ (Figures 1c and S6a). The H_2 consumption peak centered at 40 °C for $Pt(2)/CeO_2$ corresponds to 100 μmol/g of H_2 (Figure S6b), which is smaller than the amount expected from the reduction of Pt oxide clusters (205 μmol/g of H_2), assuming that all Pt species reside in the PtO_2 phase. This suggests that only larger Pt_xO_y clusters formed at a higher Pt surface density are reduced by H_2 below 50 °C.[27]

It is worth mentioning that H_2 consumption occurs over a wide temperature range for pure CeO_2, whereas it occurs over a narrower temperature range for Pt/CeO_2 (Figure 1c), with constant temperature ramp rates during the TPR. The consumption of H_2 over a wider temperature range on CeO_2 could be due to the heterogeneous reactivity of CeO_2 surfaces (many different local environments from the exposed basal planes and defect sites) and H_2 dissociation being the rate limiting step. Conversely, the narrower temperature range for H_2 consumption for Pt/CeO_2 samples is likely because H_2 dissociation occurs on Pt sites, followed by H-spillover to the CeO_2 surface. Further mechanistic insights will be discussed.

To deconvolute the influence of total Pt loading and the Pt structure on the rate of H_2 consumption, H_2-TPR for

https://doi.org/10.1021/jacsau.3c00330
JACS Au 2023, 3, 2299−2313

Pt(0.05)/CeO_2 and a physical mixture of Pt(1)/CeO_2 and CeO_2 at a mass ratio of 1:19, containing identical macroscopic Pt loadings and different Pt structures (predominantly Pt SAs at 0.05 wt % and predominantly Pt_xO_y clusters at 1 wt %), were compared (Figure 1d). T_m was lower for "Pt(1)/CeO_2:CeO_2 = 1:19" compared to Pt(0.05)/CeO_2. Hence, Pt NCs are more effective than Pt SAs in promoting H-spillover onto CeO_2 surfaces. Here, the retained promotion in the H_2 consumption rate by the entire sample in the "Pt(1)/CeO_2:CeO_2 = 1:19" physical mixture compared to pure CeO_2 suggests that the local influence of Pt on Ce−O bonds is not responsible for the broad influence of Pt on the rate of H_2 consumption on the CeO_2 surface. This is consistent with the promoted H_2 consumption rate for samples containing <1 Pt atom/CeO_2 particle as compared to pure CeO_2 (Figure 1c).

In situ XANES spectra in Figures S7−S9 show that the reduction of Pt_xO_y clusters to metallic Pt NCs occurs prior to the consumption of surface-reacting H_2 for "Pt(1)/CeO_2:CeO_2 = 1:19".[28] Here, note that the amount of Pt in the physical mixture is too small (≤0.05 wt %) so that the H_2 consumption peak associated with the reduction of Pt oxide, as observed in the in situ XANES spectra, could not be observed in the H_2-TPR curve. It is interesting that the kinetics of Pt_xO_y reduction decouples from that of H-spillover when CeO_2 particles with and without Pt are physically separated. The implications of the existence of interparticle boundaries for H_2 consumption will be discussed in more detail later.

The total amount of H_2 consumption in the surface reaction was also affected by Pt addition beyond the additional expected H_2 consumption for the reduction of Pt oxides (Table 1). It is assumed that all O atoms bound to Pt react with H_2 to form H_2O (Pt-to-O molar ratio was assumed to be 4, the greatest possible amount) and also that H bonds to Pt in a 1:1 molar ratio (e.g., Pt is covered by H). At Pt loadings ≤0.05 wt %, between 10 and 25% excess H_2 was consumed compared to the expected amount based on H_2 consumption on pure CeO_2 and the maximum amount of H_2 required to reduce and saturate Pt_xO_y. This observation is consistent with a recent report where the presence of Pt increased H_2 consumption on CeO_2 (in the form of powder catalysts) by 47%.[29] Note that the excess H_2 consumption was not observed at Pt loading ≥1 wt % (Table 1). This is because at >1 wt % Pt, the CeO_2 surface becomes significantly populated by Pt, thus decreasing the available CeO_2 surface area. For example, ∼0.45 Pt/nm^2 or ∼10% coverage of Pt on CeO_2 exists at 1 wt % Pt, which is similar to the magnitude of excess H_2 consumption observed for lower Pt loading samples.

Table 1. Amount of H_2 Consumed Estimated from H_2-TPR Curves below 500 °C, the Increased Amount of H_2 Consumed after Loading Pt Based on the Amount of H_2 Consumed on Pure CeO_2, and the Maximum Amount of H_2 Required for Pt_xO_y Reduction[a]

sample	H_2 consumed below 500°C (μmol/g)	excess H_2 consumed below 500°C (μmol/g)[b]
CeO_2	379	
Pt(0.0005)/CeO_2	472	93
Pt(0.005)/CeO_2	480	100
Pt(0.01)/CeO_2	472	91
Pt(0.02)/CeO_2	470	86
Pt(0.05)/CeO_2	467	77
Pt(1)/CeO_2	475	0[c]
Pt(2)/CeO_2	541	0[c]
Pt(1)/CeO_2:CeO_2 = 1:99	423	42

[a]Here, the Pt-to-O molar ratio is assumed to be 4.0. [b][Excess H_2 consumed] = [H_2 consumed] − [H_2 consumed on CeO_2] − [4(from O) × (the amount of Pt)] − [0.5(from Pt−H) × (the amount of Pt)]. [c][Excess H_2 consumed] is considered 0 if the estimated amount is less than 0.

Thus, based on the TPR measurements and analysis, even small amounts of Pt cause significant changes to the rate and amount of H_2 consumption by Pt/CeO_2 samples through surface reactions, even across CeO_2−CeO_2 particle boundaries, motivating analysis of the sources of these changes.

Mechanism of H_2 Activation on CeO_2 and Pt/CeO_2

H_2 can dissociate homolytically or heterolytically on CeO_2 surfaces.[30−34] Homolytic H_2 dissociation reduces two Ce^{4+} to Ce^{3+} and produces 2 hydroxyls (OH^-_{ads}), (eq 1).[31−35] Heterolytic H_2 dissociation on CeO_2 surfaces does not reduce Ce^{4+} and instead produces a hydride (H^-) on Ce^{4+} (Ce^{4+}−H^-) and an OH^-_{ads}, (eq 2).[31,32,34] Density functional theory (DFT) calculations predict that heterolytic H_2 dissociation on CeO_2 surfaces has a lower activation barrier than homolytic H_2 dissociation (Table S1) but that the homolytic product is thermodynamically preferred.[31,34,36] Therefore, it has been proposed that the heterolytic H_2 dissociation product forms initially on CeO_2 surfaces and then transforms into the homolytic product (producing an additional OH^-_{ads} and 2 Ce^{3+}) as the species equilibrate (eq 3).[16,17] Neighboring OH^-_{ads} species can react to produce H_2O_{ads} and a lattice oxygen, $O_{lattice}$ (eq 4), followed by H_2O desorption, which leaves behind V_o (eq 5).[37−39] It has also been proposed that H_2 can homolytically dissociate on neighboring Ce^{3+} species on nonstoichiometric CeO_2 surfaces (where a considerable V_o concentration exists) to produce 2 Ce^{4+}−H^- (eq 6), although these species decompose at elevated temperatures (>200 °C).[32] The barriers for these elementary steps have been studied extensively via DFT calculations (see Table S1).[30−34,36,38−42] However, the calculated energetics depend on CeO_2 surface structure, OH^-_{ads} coverage, V_o concentration, and calculation parameters, making it challenging to hypothesize the series of steps and the kinetically relevant steps for OH^-_{ads}, Ce^{3+}, and V_o formation in powdered samples under reaction conditions.

$$H_2 + 2O^{2-} + 2Ce^{4+} \rightarrow 2OH^-_{ads} + 2Ce^{3+} \quad (1)$$

$$H_2 + Ce^{4+} + O^{2-} \rightarrow OH^-_{ads} + Ce^{4+} - H^- \quad (2)$$

$$OH^-_{ads} + Ce^{4+} - H^- + Ce^{4+} \rightarrow 2OH^-_{ads} + 2Ce^{3+} \quad (3)$$

$$2OH^-_{ads} \rightarrow H_2O_{ads} + O_{lattice} \quad (4)$$

$$H_2O_{ads} \rightarrow H_2O + V_o \quad (5)$$

$$H_2 + 2Ce^{3+} \rightarrow 2Ce^{4+} - H^- \quad (6)$$

The addition of PGMs to CeO_2 has been proposed to introduce an additional H_2 reaction pathway on CeO_2 through homolytic H_2 activation on the metal and subsequent H-spillover to CeO_2, forming 2 OH^-_{ads} and 2 Ce^{3+} simultaneously (eq 7).[9,11,43,44]

$$Pt + H_2 + 2O^{2-} + 2Ce^{4+} \rightarrow Pt + 2OH^-_{ads} + 2Ce^{3+} \quad (7)$$

https://doi.org/10.1021/jacsau.3c00330
JACS Au 2023, 3, 2299−2313

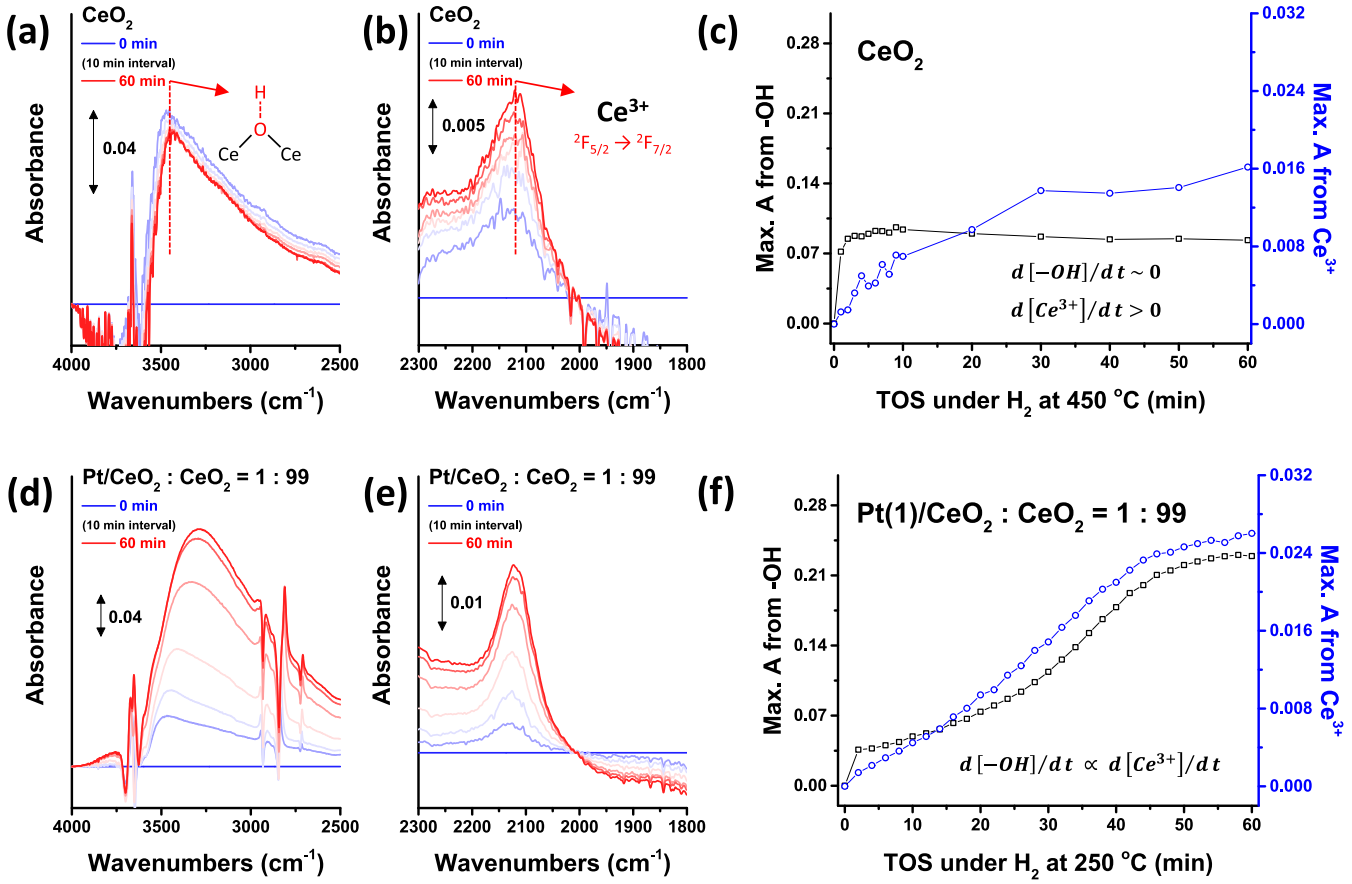

Figure 2. FTIR spectra for the (a) hydroxyl and (b) Ce^{3+} region of pure CeO_2 collected under H_2 at 450 °C and for the (d) hydroxyl and (e) Ce^{3+} region of "Pt(1)/CeO_2:CeO_2 = 1:99" collected under H_2 at 250 °C. Correlation between the maximum absorbance from surface hydroxyl and Ce^{3+} in the IR spectra of (c) pure CeO_2 from (a,b) and of (f) "Pt(1)/CeO_2:CeO_2 = 1:99" from (d,e). 10% H_2/Ar is used. The lines connecting the data points are simply to guide the eye and not model fits.

Thus, Pt can facilitate the formation of homolytic H_2 dissociation products on CeO_2 surfaces by bypassing the sequential reaction pathway proposed to occur on pure CeO_2 surfaces—heterolytic H_2 activation followed by transformation into the homolytic products. The relevance of Pt-mediated production of homolytic H_2 dissociation products on CeO_2 to the TPR results requires that H-spillover from Pt to CeO_2 is sufficiently fast across the entire CeO_2 surface to negate the relevance of direct heterolytic H_2 dissociation on CeO_2 surfaces. From eqs 1−7, the rate of formation of OH^-_{ads} ($d[OH^-_{ads}]/dt$) and Ce^{3+} ($d[Ce^{3+}]/dt$) on CeO_2 surfaces in H_2 can be expressed as eqs 8 and 9, respectively

$$d[OH^-_{ads}]/dt = 2 \times r_{homo} + r_{hetero} + r_{hetero \rightarrow homo} - 2 \times r_{H_2O} \quad (8)$$

$$d[Ce^{3+}]/dt = 2 \times r_{homo} + 2 \times r_{hetero \rightarrow homo} - 2 \times r_{homo\ on\ Ce^{3+}} \quad (9)$$

where r_{homo}, r_{hetero}, $r_{hetero \rightarrow homo}$, r_{H_2O}, and $r_{homo\ on\ Ce^{3+}}$ represent the rate of homolytic H_2 activation [rate of (1) plus rate of (7)], heterolytic H_2 activation [rate of (2)], transformation of heterolytic products to homolytic products [rate of (3)], H_2O formation [rate of (4), assuming the rate of (5) is quasi-equilibrated], and homolytic H_2 activation on Ce^{3+} near V_o [rate of (6)]. We note that the reverse of (6) has also been proposed to produce H_2 from hydride decomposition, and this will be discussed later.[32,36]

To interrogate the kinetics, mechanisms, and kinetically relevant steps associated with H_2 reactions on CeO_2 and Pt/CeO_2 surfaces, the relative concentrations of surface hydroxyls, [OH^-_{ads}], and Ce^{3+}, [Ce^{3+}], were measured using in situ FTIR while flowing 10% H_2 at constant temperatures (250, 350, or 450 °C) over materials that were pre-oxidized in situ with 10% O_2 for 30 min at 400 °C. In situ FTIR provides the distinct ability, compared to other characterization approaches, to follow both [OH^-_{ads}] and [Ce^{3+}] simultaneously with a time resolution of <1 min at atmospheric pressure and above.[45] Details on the FTIR spectra acquisition methodology, which facilitates quantitative comparison of spectra collected from different samples, are provided in Supporting Information Discussion II (Figures S10−S13).

The consumption of H_2 via surface reactions on pure CeO_2 was complete at ~ 450 °C in TPR measurements (Figures 1 and S14). When CeO_2 was exposed to H_2 at a constant temperature of 450 °C, in situ IR evidenced increases in the intensity of bands assigned to OH^-_{ads} (3000−3500 cm^{-1}) and the forbidden $^2F_{5/2}$-to-$^2F_{7/2}$ electronic transition of Ce^{3+} (2130 cm^{-1}) (Figure 2a,b), respectively.[46−49] See Supporting Information Discussion III for the assignment of the electronic transition of Ce^{3+}. Changes in the intensity of these two bands as a function of time are displayed in Figure 2c, where [OH^-_{ads}]

https://doi.org/10.1021/jacsau.3c00330
JACS Au 2023, 3, 2299−2313

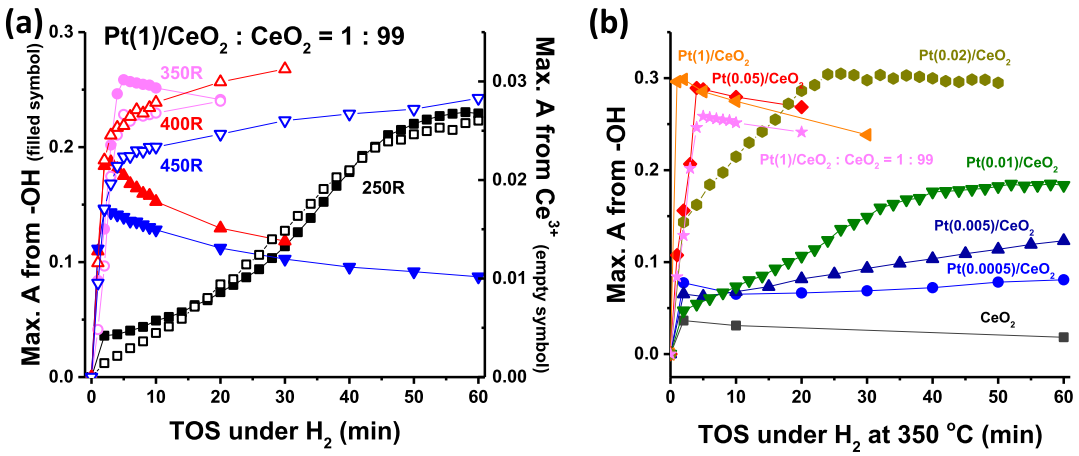

Figure 3. (a) Change in the maximum absorbance from surface hydroxyl and Ce^{3+} estimated from IR spectra of "Pt(1)/CeO_2:CeO_2 = 1:99" collected under H_2 at 250, 350, 400, and 450 °C. Filled and empty symbols represent the absorbance from surface hydroxyl and Ce^{3+}, respectively. (b) Change in the maximum absorbance from surface hydroxyl estimated from IR spectra collected under H_2 at 350 °C on pure CeO_2 and Pt/CeO_2 with different Pt loadings. 10% H_2/Ar was used, which equals to 76 Torr of H_2. The lines connecting the data points are simply to guide the eye and not model fits.

saturates within ~5 min, while $[Ce^{3+}]$ increases consistently for more than 60 min.

The time-dependent evolution of $[OH^-_{ads}]$ and $[Ce^{3+}]$ provide insights into the mechanism of H_2 reactions on CeO_2 surfaces. First, $r_{homo\ on\ Ce^{3+}}$ (6) is assumed to be 0 as $[Ce^{3+}]$ did not change when the sample was purged with Ar after reaction with H_2 at 450 °C (Figure S15). This suggests that hydrides formed by homolytic activation on Ce^{3+} are not stable at 450 °C, and thus, this reaction has no net forward rate under the explored conditions. In addition, it was recently reported that the intensity of the IR band associated with Ce^{3+} is linearly proportional to the amount of H_2O produced during reaction with H_2.[50] This suggests that the reverse reaction of (6) has a negligible rate as this step does not produce H_2O.[23,51] Therefore, $d[Ce^{3+}]/dt$ in eq 9 can be simplified to eq 10

$$d[Ce^{3+}]/dt = 2 \times r_{homo} + 2 \times r_{hetero \rightarrow homo} \quad (10)$$

The larger initial rate of $[OH^-_{ads}]$ formation compared to $[Ce^{3+}]$ formation (Figure 2c) suggests that r_{hetero} is initially larger than the sum of r_{homo} and $r_{hetero \rightarrow homo}$. This is consistent with the hypothesis from theoretical calculations that H_2 initially heterolytically dissociates on CeO_2 and that Ce^{3+} formation proceeds via transformation of heterolytic H_2 dissociation products into homolytic H_2 dissociation products. From eq 8, the observation of pseudo-steady-state $[OH^-_{ads}]$ after ~5 min of $(d[OH^-_{ads}]/dt \sim 0)$ leads to eq 11

$$2 \times r_{H_2O} \sim 2 \times r_{homo} + r_{hetero} + r_{hetero \rightarrow homo} \quad (11)$$

r_{homo} and r_{hetero} are assumed to be 0 once $d[OH^-_{ads}]/dt \sim 0$ because H_2 consumption on CeO_2 is completed quickly at 450 °C (Figures S16 and S17). Since $d[Ce^{3+}]/dt > 0$ while $d[OH^-_{ads}]/dt \sim 0$, eq 10 suggests that $r_{hetero \rightarrow homo}$ is >0. This then leads to the conclusion that both $d[Ce^{3+}]/dt$ and r_{H_2O} are limited by $r_{hetero \rightarrow homo}$ on CeO_2 at 450 °C in H_2. $r_{hetero \rightarrow homo}$ limiting r_{H_2O} suggests that H_2 consumption occurs before H_2O formation on pure CeO_2, which is consistent with previous reports.[51]

Similar measurements were performed on "Pt(1)/CeO_2:CeO_2 = 1:99", where Pt NCs exist on 1 out of every 100 CeO_2 particles and the consumption of surface-reacting H_2 is completed at 250 °C in H_2-TPR (Figure S14). IR spectra collected at 250 °C under a H_2 flow show that $[OH^-_{ads}]$ and $[Ce^{3+}]$ increased simultaneously (Figure 2d,e), distinct from the behavior of pure CeO_2. This correlation ($d[OH^-_{ads}]/dt = \alpha \times d[Ce^{3+}]/dt$; α is constant) requires that r_{homo} be much larger than r_{hetero} or r_{H_2O} (eqs 8 and 9). This indicates that Pt NCs promote the spillover of homolytic H_2 dissociation products onto the CeO_2 surface (eq 7) but that the rate of H_2O formation is slow compared to the rate of H-spillover at 250 °C. This is consistent with previous reports that H_2 consumption occurs on PGM-supported CeO_2 surfaces before H_2O evolution during H_2-TPR on high-surface area catalysts.[23] Further, the consistent formation rates of $[OH^-_{ads}]$ and $[Ce^{3+}]$ until they reach saturation suggests that homolytically dissociated H_2 on Pt spills over to the entire CeO_2 surface (even to CeO_2 particles not containing Pt) at a faster rate than heterolytic H_2 activation directly on CeO_2. When the H_2 exposure temperature on "Pt(1)/CeO_2:CeO_2 = 1:99" was increased to >350 °C, both $[OH^-_{ads}]$ and $[Ce^{3+}]$ reached maxima within 1−2 min, and subsequently, $[OH^-_{ads}]$ decreases as a function of time, suggesting that H_2O formation proceeds (Figure 3a).

Similar experiments were executed for Pt(0.01)/CeO_2, where Pt is primarily atomically dispersed as single atoms (Figures S2 and S3). Close correlation between $d[OH^-_{ads}]/dt$ and $d[Ce^{3+}]/dt$ was again observed (Figure S18). While this may indicate that Pt SAs promote the spillover of homolytic H_2 dissociation products to the CeO_2 surface, there is a debate in the literature on whether Pt SAs can promote homolytic H_2 dissociation.[52−54] We cannot rule out the possibility that Pt NCs present in a low concentration in Pt(0.01)/CeO_2 are responsible for the homolytic H_2 dissociation. Regardless, $d[OH^-_{ads}]/dt$ and $d[Ce^{3+}]/dt$ were larger for samples having a larger concentration of Pt NCs, even with identical nominal Pt loadings (Figure S18). This is consistent with Pt NCs activating H_2 at faster rates than Pt SAs, as observed in Figure 1d and reported previously.[55−57]

The in situ FTIR data provide evidence of other changes to H_2 surface chemistry on CeO_2 caused by Pt. First, "Pt(1)/CeO_2:CeO_2 = 1:99" showed ~25% higher saturation of $[Ce^{3+}]$

https://doi.org/10.1021/jacsau.3c00330
JACS Au 2023, 3, 2299−2313

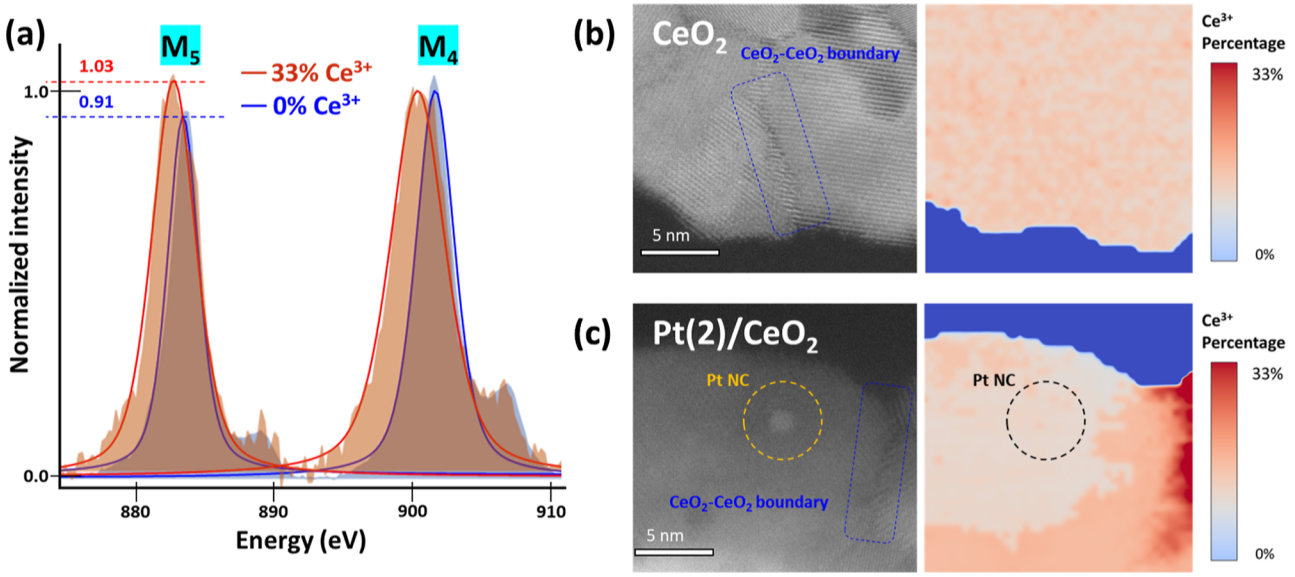

Figure 4. (a) Representative EEL spectra with different Ce^{3+} concentrations after PCA, power law, and arctan background subtraction, normalized to the Ce M_4 peak height. Processed data are represented by the shaded regions, and the fitted Voigt peaks are represented by the solid lines. HAADF-STEM and EELS mapping images of (b) pure CeO_2 after in situ reduction at 450 °C for 60 min and (c) Pt(2)/CeO_2 with Pt NCs after in situ reduction at 400 °C for 60 min. 10 Torr of H_2 is used. In the EELS maps, a gradual change of the color map from blue to red indicates a gradual increase in Ce^{3+} concentration.

compared to that of pure CeO_2 (Figure S19), which is consistent with the increased H_2 consumption observed during TPR (Table 1). The agreement between the IR analysis of relative $[Ce^{3+}]$ and the TPR data provides confidence in conclusions drawn from quantitative comparisons of the magnitudes of IR signatures for different samples. Based on this justification, the magnitude of $[OH^-_{ads}]$ can be compared between samples and H_2 exposure temperatures to understand how Pt influences saturation $[OH^-_{ads}]$.

When CeO_2 was exposed to 76 Torr H_2, the magnitude of the integrated OH^-_{ads} IR absorbance increased from 0.025 to ∼0.09 as exposure temperature increased from 350 to 450 °C (Figure S20). The integrated OH^-_{ads} absorbance only slightly increased to 0.11 as H_2 pressure was increased to 760 or 5320 Torr (Figure S21). This indicates that the integrated absorbance of ∼0.1 is saturation OH^-_{ads} coverage on CeO_2 due to H_2 exposure. Alternatively, the integrated OH^-_{ads} absorbance during exposure to 76 Torr H_2 at 350 °C was consistently 0.25−0.3 on various Pt/CeO_2 samples (Figure 3b). Increasing the H_2 exposure temperature above 350 °C caused a decrease in the intensity of the OH^-_{ads} band, associated with H_2O formation (Figure 3a).

The >2× increase in saturation OH^-_{ads} coverage on Pt/CeO_2 samples as compared to pure CeO_2 is consistent with the different mechanism of H_2 activation (homolytic vs heterolytic) and the kinetic relevance of converting the heterolytic products to homolytic products for H_2O formation on pure CeO_2; homolytic activation produces $2OH^-_{ads}$ per H_2, while heterolytic activation produces $1OH^-_{ads}$ and 1 $Ce^{4+} - H^-$. If $r_{hetero\rightarrow homo}$ were faster than r_{H_2O} on CeO_2, then the integrated OH^-_{ads} absorbance should approach values observed for Pt/CeO_2 (the OH^-_{ads} concentration should double in converting the heterolytic product to the homolytic product) given that the IR data at temperatures greater than 350 °C demonstrate that H_2O formation is kinetically feasible.

The in situ FTIR results demonstrate a number of important findings: (1) H_2 activation on pure CeO_2 occurs via heterolytic H_2 dissociation, followed by equilibration to the homolytic product, before H_2O formation proceeds; (2) on pure CeO_2, the rates of Ce^{3+} and H_2O formation are limited by the rate of conversion of the heterolytic H_2 dissociation product to the homolytic product; and (3) H_2 activation on Pt/CeO_2 (even in samples with Pt residing on only 1% of the CeO_2 particles) occurs exclusively via homolytic H_2 dissociation on Pt, followed by rapid and far-reaching H-spillover to CeO_2 at rates much faster than H_2O formation, allowing for a significant increase in OH^-_{ads} coverage on Pt/CeO_2 (more than 2×) as compared to pure CeO_2. The results also indicate that Pt indirectly promotes H_2O (and V_o) formation at locations remote from Pt via H-spillover by mitigating the kinetic limitation on pure CeO_2 of converting the heterolytic H_2 dissociation products to homolytic H_2 dissociation products. This is also consistent with previous reports that the addition of PGMs on CeO_2 surfaces promotes H_2O evolution at a lower temperature during H_2-TPR runs.[23,58,59]

It is worth mentioning that a coincidence of $[OH^-_{ads}]$ and $[Ce^{3+}]$ for Pt/CeO_2, delayed Ce^{3+} formation as compared to OH^-_{ads} on CeO_2, ∼2× lower saturation $[OH^-_{ads}]$ for CeO_2 than for Pt/CeO_2, and OH^-_{ads} on CeO_2 devoid of Pt over a micrometer away from Pt were recently observed in XPS experiments performed at lower H_2 pressures on similar samples (0.8 Torr of H_2 was used in the XPS studies of Pt-loaded CeO_2 films with ∼10 nm grain sizes, as compared to 75 Torr of H_2 used here in TPR and FTIR experiments). However, no mechanistic discussions associated with the origin of these behaviors apart from the prevalence of H-spillover were provided.[10] The agreement between specific behaviors of $[OH^-_{ads}]$ and $[Ce^{3+}]$ suggests that the mechanistic details proposed here for the influence of Pt on CeO_2 surface reactions with H_2 are valid over a wide range of H_2 chemical potentials.

https://doi.org/10.1021/jacsau.3c00330
JACS Au 2023, 3, 2299−2313

Ce^{3+} Distribution on CeO_2 Surfaces

It is evident from Figures 2 and 3 that the addition of Pt to CeO_2 lowered the temperature for H_2 activation and H_2O formation and increased the saturation OH^-_{ads} coverage on CeO_2. Further, these influences spread far from the Pt−CeO_2 interfaces. However, the spatial distribution of OH^-_{ads} and Ce^{3+} and the source of increased H_2 consumption and Ce^{3+} formation on Pt/CeO_2 samples are unclear. To address these questions, the spatial distribution of Ce^{3+} was measured using in situ EELS at a high spatial resolution.[60] EELS can distinguish Ce ions with different oxidation states as the $M_{4,5}$ edges appear at a lower energy as Ce^{4+} is reduced to Ce^{3+} and since the relative intensity ratio of the M_5 to M_4 edges (I_{M_5}/I_{M_4}) is 1.31 for Ce^{3+} and 0.91 for Ce^{4+} (Figure 4a).[15,61,62] In this study, the spatial distribution of Ce^{4+} and Ce^{3+} after different thermal treatments was estimated from I_{M_5}/I_{M_4}. CeO_2 was reduced in situ with H_2 at 450 °C, while Pt/CeO_2 was reduced in situ with H_2 at 400 °C to ensure complete H_2 consumption in <60 min (the time used in between EELS collection on oxidized and reduced samples). The experimental procedures and data analysis associated with the EELS measurements are summarized in Figures S22 and S23.

The spatially resolved EELS data for pure CeO_2 following exposure to 10 Torr of H_2 for 60 min at 450 °C shows that Ce^{3+} was homogeneously distributed (Figure 4b, red regions have higher concentrations of Ce^{3+}). In contrast, when Pt(2)/CeO_2 (containing Pt NCs) was exposed to 10 Torr of H_2 at 400 °C for 1 h, Ce^{3+} was formed heterogeneously across the sample (Figures 4c and S24). By correlation of EELS with TEM images, it is seen that a large fraction of Ce^{3+} is associated with CeO_2−CeO_2 interparticle interfaces rather than near Pt NCs, distinct from reports in the literature that hypothesize that reduced Ce species localize at PGMs.[14] Similar to Pt(2)/CeO_2, Ce^{3+} formed heterogeneously throughout the sample when Pt(0.01)/CeO_2 (containing mostly Pt SAs) was exposed to H_2 under similar conditions (Figure S25). Thus, Pt addition changed the spatial distribution of Ce^{3+} in powder CeO_2 samples following H_2 exposure.

The spatially averaged Ce^{3+} concentrations were quantified for pure CeO_2, Pt(0.01)/CeO_2, and Pt(2)/CeO_2 samples from the EELS data following H_2 exposure and agreed with estimates from H_2-TPR and H_2-FTIR (Table 2, see Supporting Information Discussion IV for details of calculation). Note that the bulk Ce^{3+} concentration of 8.1 and 16.3% for pure CeO_2 and Pt(0.01)/CeO_2 in Table 2 represent the Ce^{3+} surface coverage of 0.53 and 1.07 monolayers, respectively (assuming that CeO_2 exposes only (111) surface, see Supporting Information Discussion IV for details of calculation). This suggests that surface Ce^{4+} remote from Pt (the Pt coverage is very low) were reduced to Ce^{3+} due to Pt promoting H-spillover, although because of the high Ce^{3+} mobility at these temperatures, the formation of Ce^{3+} at Pt/CeO_2 interfaces followed by diffusion to heterogeneous locations across the sample cannot be ruled out. The EELS data cannot distinguish whether Ce^{3+} is associated with OH^-_{ads} or V_o. However, since both CeO_2 and Pt/CeO_2 samples were reduced with H_2 at elevated temperatures for 60 min, it is likely that some fraction of OH^-_{ads} condensed to produce H_2O and V_o, as deduced from the IR analysis. The EELS maps indicate that a large fraction of Ce^{3+} (and likely associated V_o) localize at and around the boundaries between CeO_2 particles when Pt is added, distinct from the common assumption of Ce^{3+} localization around Pt and from the behavior of pure CeO_2.

Table 2. Comparison of the Estimated Ce^{3+} Concentrations from In Situ EEL Spectra vs H_2-TPR Curves and In Situ H_2-FTIR Spectra[a]

sample		Ce^{3+} concentration[b]	
		from EELS (%)[c]	from TPR and FTIR (%)
CeO_2	before reduction	0.3	0[d]
	after reduction	5.9	8.1[e]
Pt(0.01)/CeO_2	before reduction	2.3 ± 0.5	0[d]
	after reduction	11.4 ± 3.0	16.3[f]
Pt(2)/CeO_2	before reduction	2.4 ± 0.2	0[d]
	after reduction	10.8 ± 2.9	18.7[f]

[a]See Supporting Information Discussion IV for details of calculation. [b]The Ce^{3+} concentration is calculated with respect to all Ce (bulk and surface) in the sample. [c]For EELS, CeO_2 was in situ reduced at 450 °C for 1 h and Pt/CeO_2 was in situ reduced at 400 °C for 1 h in10 Torr H_2. [d]The Ce^{3+} concentration is determined to be 0 because the single-beam intensity from Ce^{3+} in the FTIR spectra was 0 before reduction with H_2. [e]The absorbance from Ce^{3+}, estimated from H_2-FTIR spectra after H_2 reduction at 450 °C for 60 min with 75 Torr of H_2, is used to estimate the Ce^{3+} concentration on pure CeO_2. This is because the Ce^{3+} concentration slowly increases over time (Figure 2c). [f]Ce^{3+} % on Pt/CeO_2 samples is estimated assuming that all the H_2 reacting with the surface of Pt/CeO_2 (from H_2-TPR curves) is converted to −OH since Pt promoted the homolytic H_2 dissociation and subsequent H-spillover.

Another interesting observation from the EELS data in Figures 4, S24, and S25 is that for Pt(2)/CeO_2, the Ce^{3+} concentration is higher on CeO_2 surfaces near the boundaries between CeO_2 particles as opposed to "free" CeO_2 surfaces. This suggests that both Pt addition and interactions between neighboring CeO_2 particles are required to produce high concentrations of Ce^{3+} at CeO_2 surfaces following H_2 exposure at high temperatures and that interparticle CeO_2 interactions may be responsible for the excess H_2 consumption (and associated Ce^{3+} concentration) seen for Pt/CeO_2 samples as compared to pure CeO_2.

Irreversible Changes at the Boundaries between CeO_2 Particles by Spillover H

The observation of Ce^{3+} localization around CeO_2 interparticle boundaries for Pt/CeO_2 samples following H_2 exposure suggests the potential for reconstruction at these locations. To analyze potential reconstruction, H_2-TPR was subsequently executed after an initial reduction-oxidation pretreatment cycle. In Figure 5a, it is observed that the second TPR shows no changes as compared to the first TPR for pure CeO_2. Alternatively, the T_m for "Pt(1)/CeO_2:CeO_2 = 1:99" occurs at >200 °C lower temperature in the second TPR (Figure 5b). The lower T_m in the second TPR could be due to a milder oxidation of Pt, which could lead to the formation of metallic Pt at a lower temperature and, thus, increased H_2 consumption at a lower temperature. However, when Pt(2)/CeO_2 was exposed to H_2 at 400 °C, diluted with untreated CeO_2 in a 1:99 mass ratio, and oxidized at 350 °C, the consumption of surface-reacting H_2 occurred at a higher temperature than that of the re-oxidized "Pt(1)/CeO_2:CeO_2 = 1:99" (Figure S26). Moreover, the decrease in T_m in sequential TPR cycles was also observed on Pt(0.01)/CeO_2 that has mostly Pt SAs (Figure S27), although Pt SAs do not significantly sinter under H_2 at 350 °C at these weight loadings (Figure S3).[20] These

https://doi.org/10.1021/jacsau.3c00330
JACS Au 2023, 3, 2299−2313

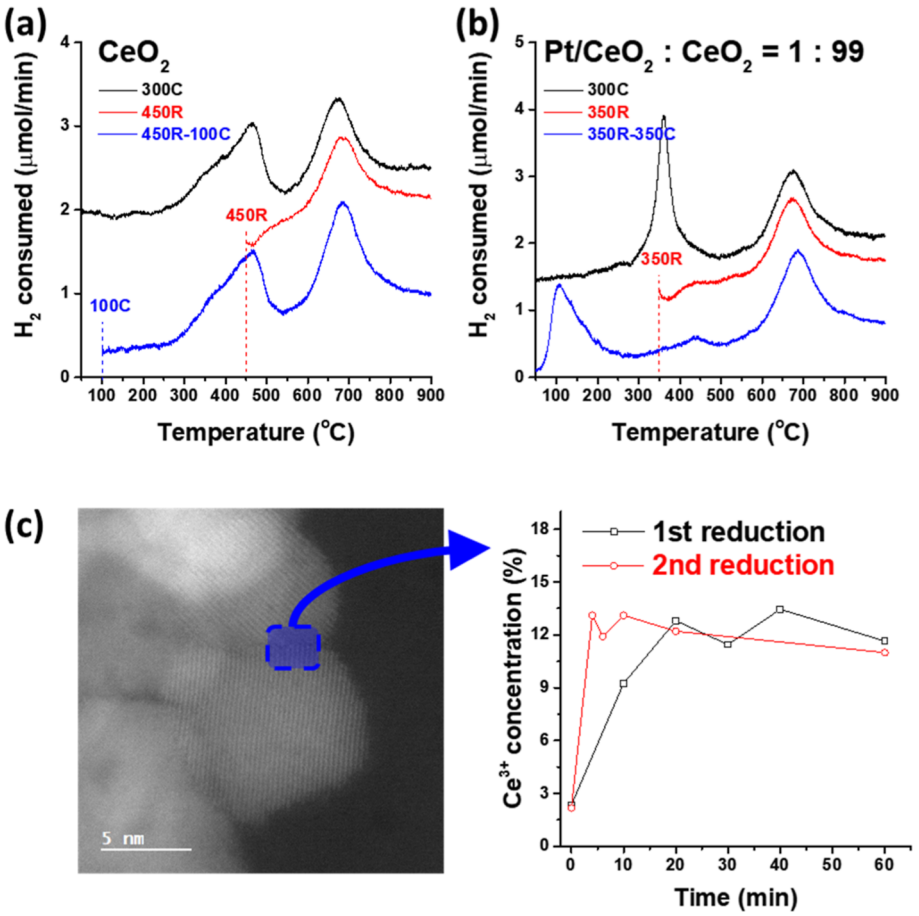

Figure 5. H_2-TPR curves of (a) pure CeO_2 and (b) "Pt(1)/CeO_2:CeO_2 = 1:99" (i) after oxidation at 300 °C, (ii) after reduction at (a) 450 °C or (b) 350 °C, and (iii) after (a) reduction at 450 °C followed by re-oxidation at 100 °C or after (b) reduction at 350 °C followed by re-oxidation at 350 °C. (c) Rate of Ce^{3+} formation at the boundary of Pt(1)/CeO_2 particles during the 1st and 2nd reductions by using EELS. Sample was re-oxidized at 400 °C after reduction at 400 °C to measure the rate of the 2nd reduction.

results indicate that modified Pt reducibility is not the source of the irreversible change in T_m for Pt/CeO_2 during sequential TPR cycles.

The rate of Ce^{3+} formation on "Pt(1)/CeO_2:CeO_2 = 1:99" during sequential isothermal H_2 exposures with re-oxidation in between was also measured via FTIR (Figure S28) and EELS (Figure 5c). In agreement with the TPR data, FTIR data evidenced faster formation rates of OH^-_{ads} and Ce^{3+} during the second H_2 exposure. EELS also showed that Ce^{3+} is formed at a faster rate at the boundaries between CeO_2 particles during the second H_2 exposure (Figure 5c). These results support the hypothesis that spillover H from Pt and the resulting high OH^-_{ads} coverage that is unique to Pt/CeO_2 are correlated with the localization of Ce^{3+} near the boundaries between CeO_2 particles, which resulted in irreversible changes to the H_2 consumption kinetics.

To suppress the formation of boundaries between CeO_2 particles and examine the influence on the rate of H_2 consumption, CeO_2 and Pt(0.05)/CeO_2 were diluted with γ-Al_2O_3 (diameter, 5 nm) in 1:1 or 1:3 mass ratios (Figure 6a). As an irreducible oxide, γ-Al_2O_3 can serve as an insulator against H-spillover between CeO_2 particles as the inherent rate of H-spillover on γ-Al_2O_3 is low and the small particle size creates physical barriers between CeO_2 particles.[9] TPR of pure CeO_2 was not affected by dilution with Al_2O_3 (Figure 6a). On the other hand, T_m for Pt/CeO_2 shifted to higher temperatures as the dilution ratio with Al_2O_3 increased (Figure 6b). Also, the amount of H_2 consumed in the TPR decreased to that expected for pure CeO_2 as the dilution ratio increased (Table S2). Although Al_2O_3 may accept some spillover H from Pt,[9] the effect of Al_2O_3 suppressing the formation of the CeO_2–CeO_2 boundary appears to be more critical in determining the rate and amount of H_2 consumption.

Fast Fourier transforms (FFTs) of STEM images of collections of pure CeO_2 and Pt/CeO_2 particles before and after in situ reactions with H_2 were generated to investigate physical changes at the interfaces between CeO_2 particles (Figure 6c). FFTs of STEM images containing CeO_2 particles with randomly oriented grains exhibit complex diffraction patterns due to the electron beam scattering off variously oriented crystal planes, whereas collections of oriented particles produce simpler diffraction patterns similar to single-crystal materials (Figure S29). FFTs of pure CeO_2 particles exhibited a variety of diffraction patterns before and after in situ reaction with H_2 at 450 °C (Figure 6c). Prior to exposure to H_2, Pt/CeO_2 particles similarly show a wide variety of diffraction patterns. However, the number of observed diffraction patterns decreased for Pt/CeO_2 after in situ reaction with H_2 at 400 °C (Figure 6c), although no signs of CeO_2 aggregation were observed from XRD patterns and surface area measurements (Figure S30). The change in the diffraction pattern for Pt/CeO_2 following exposure to H_2 at

https://doi.org/10.1021/jacsau.3c00330
JACS Au 2023, 3, 2299–2313

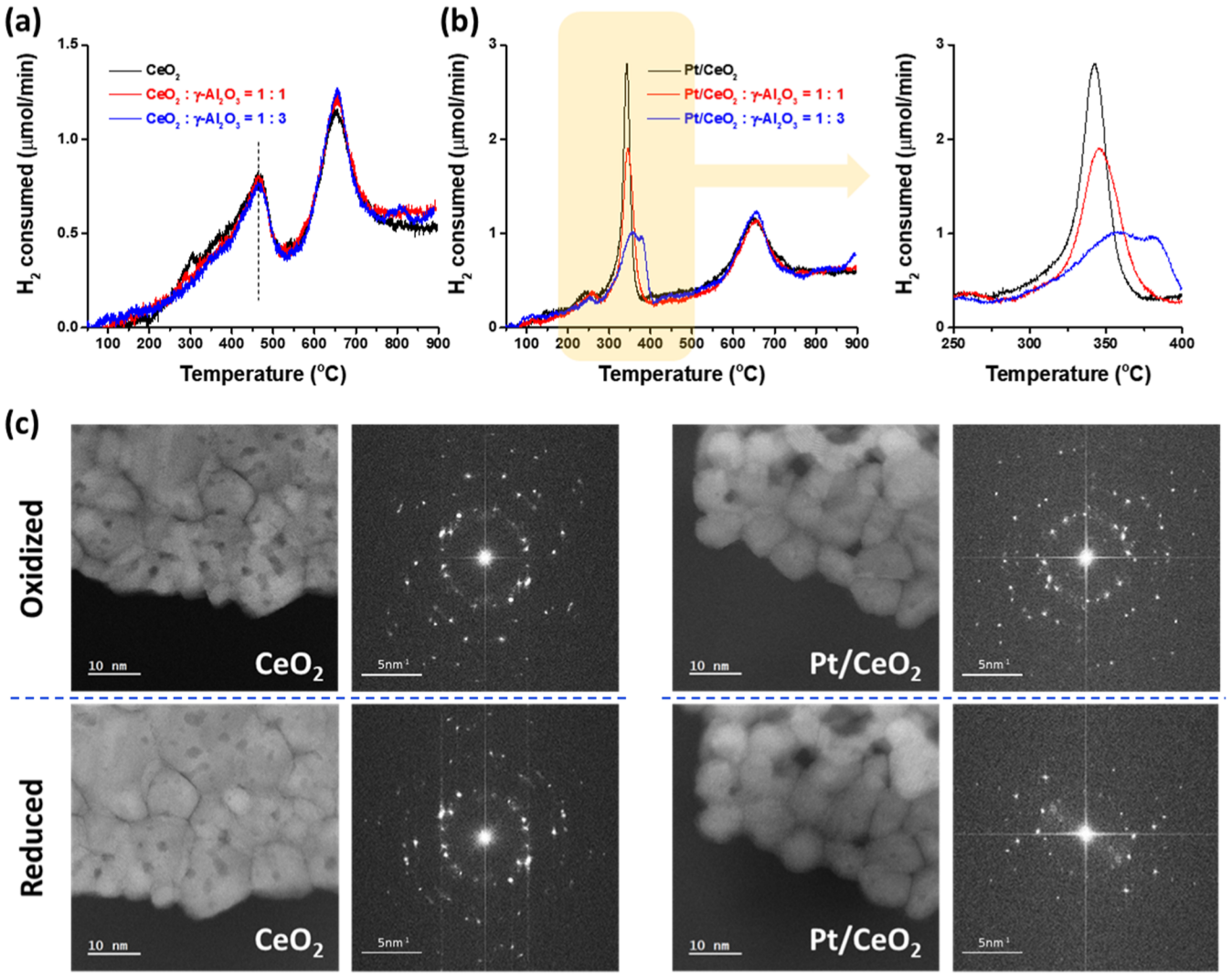

Figure 6. H_2-TPR curves of (a) CeO_2 or (b) Pt(0.05)/CeO_2 are collected after dilution with γ-Al_2O_3 in a 1:1 or 1:3 mass ratio. (c) STEM images and FFTs for the corresponding region of pure CeO_2 and Pt/CeO_2 before and after in situ reduction with H_2 at 450 °C for pure CeO_2 and at 400 °C for Pt/CeO_2.

elevated temperatures suggests re-orientation of the CeO_2 particles to produce aligned grains. Note that the lattice alignment between CeO_2 particles (which is often termed oriented attachment and is noted to have relatively small activation barriers[63,64]) and the removal of some of the surface oxygen are the prerequisites for CeO_2 sintering.[65−67] The underlying principle of particle sintering is to lower the surface energy. Thus, it seems likely that particle orientation in the Pt/CeO_2 samples during H_2 exposure is thermodynamically driven by minimizing surface energy and that the high OH^-_{ads} coverage caused by H-spillover from Pt facilitates this process.[65−67] These results also suggest that the interaction between CeO_2−CeO_2 particles with aligned interfaces may facilitate faster kinetics of H_2 consumption and the increased total H_2 consumption seen in Pt/CeO_2 samples.

DISCUSSION

This work demonstrates that the addition of Pt to CeO_2 particles changes the reaction mechanism of H_2 with the CeO_2 surfaces in powder catalysts and facilitates broad reconstruction of the system. H_2 is predominantly heterolytically dissociated on pure CeO_2 surfaces (eq 2), and H_2O evolution is limited by the transformation of heterolytic H_2 dissociation products into homolytic products (eq 3). On the other hand, H_2 homolytically dissociates on Pt in Pt/CeO_2 at a lower temperature compared to on pure CeO_2 surfaces, followed by rapid H-spillover to the CeO_2 surface, even across CeO_2−CeO_2 interparticle contacts (eq 7). This results in more than twofold higher saturation surface OH^-_{ads} coverage on Pt/CeO_2 compared to pure CeO_2 (Figure 3). The direct production of the homolytic dissociation product enables H_2O evolution on Pt/CeO_2 at a lower temperature compared to that on pure CeO_2,[19,46,47] since H_2O evolution is no longer limited by the transformation of heterolytic products into homolytic products as is the case for pure CeO_2. Interestingly, following H_2 exposure to Pt/CeO_2, the accumulation of Ce^{3+} and V_o was observed at the boundary between CeO_2 particles instead of at Pt−CeO_2 interfaces. That is, the impact of Pt is global across the whole sample (both in terms of H-spillover and promoted V_o formation) and not just at the Pt−CeO_2 interface.

Here, note that the H-spillover can occur across CeO_2 particles in physical contact, from CeO_2 particles containing Pt to Pt-free CeO_2 particles (e.g., in "Pt(1)/CeO_2:CeO_2 = 1:99"). This allowed us to separate the roles of the Pt structure,

https://doi.org/10.1021/jacsau.3c00330
JACS Au 2023, 3, 2299−2313

Pt−CeO_2 contact, and CeO_2−CeO_2 interactions in H_2 reactions with CeO_2 surfaces. The rate of interparticle H-spillover could depend on many different variables related to CeO_2 particles (e.g., the contact area or the extent of lattice alignment of CeO_2 particles). However, detailed insights into interparticle H-spillover are lacking and further investigation is required.

An interesting aspect of our findings is that the inclusion of insulating physical spacers (small Al_2O_3) between CeO_2 particles containing Pt increases the T_m and decreases the amount of H_2 consumed in TPR experiments (Figure 6b and Table S2). This indicates that the lattice alignment of CeO_2 particles during the exposure to H_2 at elevated temperatures that is observed for Pt/CeO_2 must occur during the H_2 consumption process, and this alignment promotes the rate of low-temperature H_2 consumption and provides a mechanism for enhanced H_2 consumption. It is noted that the activation barrier for the oriented attachment of CeO_2 particles is reported to be 54 kJ/mol for CeO_2 particles with a diameter of ∼2 nm and 95 kJ/mol for CeO_2 particles with a diameter of ∼60 nm, suggesting that the oriented attachment of the 8 nm CeO_2 particles studied here would have accessible barriers at the T_m observed in our studies.[64−66] It is presumed that the CeO_2 surfaces at the aligned grains of CeO_2 particles can stabilize higher concentrations of surface hydroxyls as well as Ce^{3+} and are inherently more reactive. It is also possible that the rate of H-spillover at the aligned boundaries is faster than on misaligned grains, thus promoting the rate of H_2 consumption on Pt/CeO_2.

The alignment of CeO_2 particles after reduction could be related to the accumulation of V_o at the boundaries. It has been reported that the presence of V_o at grain boundaries (GBs) of CeO_2 with abrupt structural and chemical inhomogeneities can relax the local structural distortion and stabilize the GB structure.[68,69] GBs are defects in oxide crystals and distinct from boundaries formed between oxide nanoparticles studied here because the nanoparticles do not form contiguous interfaces. However, they share similarities in that both boundaries exhibit abrupt structural and chemical inhomogeneities. Therefore, we hypothesize that the role of V_o at the boundary between CeO_2 particles is similar to the role of V_o at GBs. That is, V_o localized at the boundaries of CeO_2 particles may induce significant surface reconstruction that stabilizes the oxygen nonstoichiometric CeO_2 (e.g., oxygen-deficient) surfaces facing each other. This surface reconstruction may accompany the oriented attachment of CeO_2 particles since CeO_2 particles are mobile, and the structural inhomogeneity is loosened when CeO_2 grains align with each other.

However, it is unclear whether V_o promotion of the lattice alignment of CeO_2 particles is a direct result of the presence of V_o at the boundaries between CeO_2 particles or the indirect result of V_o changing the energetics of H_2O formation/desorption steps. The formation of V_o on CeO_2 surfaces proceeds in 2 steps: (i) recombination of surface hydroxyls (eq 4) followed by (ii) H_2O desorption (eq 5). V_o stabilizing the boundaries of nonstoichiometric CeO_2 particles suggests that the surface energy of the product from (i) and (ii) becomes lower. Therefore, it might be possible that step (i) becomes favored at the aligned boundary of CeO_2 particles as a result of a change in reaction energetics. In this case, the high hydroxyl coverage on Pt/CeO_2 attained by the activation of homolytic H-spillover from Pt would be sufficient to promote the alignment or oriented attachment of CeO_2 particles. The accelerated H_2 consumption over "Pt(1)/CeO_2:CeO_2 = 1:99" after reacting with H_2 at 250 °C, at which temperature H_2O evolution occurs very slowly, supports this inference (Figure S28), although this requires more rigorous investigation.

While the EELS mapping suggests that Ce^{3+} and V_o accumulate at CeO_2−CeO_2 boundaries after reacting with H_2 at 400 °C, the question remains as to where H_2O formation occurs in Pt/CeO_2. H_2O formation and V_o formation could occur directly at the CeO_2−CeO_2 boundaries, but could also occur at the Pt−CeO_2 interface followed by migration of V_o to the CeO_2−CeO_2 boundaries. Although more research is needed to understand which of these two pathways is dominant, it should be emphasized that the H_2 activation step and the V_o formation step may not necessarily occur in the same location. For example, the formation of H_2O may occur at the CeO_2−CeO_2 boundaries due to the increased concentration of surface hydroxyls that migrated from Pt through H-spillover. It would be interesting to compare the Ce^{3+} distribution after reacting with a reducing agent known to be less mobile than H (e.g., CO or hydrocarbons) to better understand how CeO_2−CeO_2 interparticle boundaries participate in the V_o formation step.

It is worth emphasizing that this study was conducted on a powder catalyst with a high surface area in which CeO_2 particles form interacting boundaries between each other. This is different from the model structures commonly studied in surface science studies, where the surface extends infinitely and forms no CeO_2−CeO_2 boundaries or interfaces. It will be important to consider these materials gaps when linking the conclusions of surface science analyses with the findings from this study and other studies on high-surface area CeO_2 materials. For example, a surface science study conducted on a model surface where Pt was dispersed on a CeO_2(111) film grown on a Cu(111) single crystal reported that H-spillover from Pt to CeO_2 occurs primarily below 25 °C, and oxygen spillover from CeO_2 to Pt occurs more preferentially above 150 °C.[11] These conclusions are somewhat different from those reached in the current study. It is possible that the presence of boundaries between CeO_2 particles in the Pt/CeO_2 powder altered the role of Pt in influencing the CeO_2 surface reactions with H_2. Our observation that Ce^{3+} is preferentially formed at and around the boundary between CeO_2 particles (Figure 4) and that both the rate and amount of H_2 consumption on Pt/CeO_2 decrease when the formation of boundaries between CeO_2 particles is suppressed (Figure 6b and Table S2) support this inference. Recently, we also found that the Pt sintering is promoted when the lattice of neighboring CeO_2 particles are aligned.[70] That is, the boundary between CeO_2 particles not only affects how H_2 reacts with Pt/CeO_2 but also plays an important role in determining the thermal stability of dispersed Pt species. Although the boundaries between support particles are often neglected when constructing model structures, a more in-depth consideration of the boundaries between support particles may be important for understanding the properties of powder heterogeneous catalysts.

CONCLUSIONS

In this contribution, reactions of H_2 on high-surface area Pt/CeO_2 powder catalysts were examined. H_2 is predominantly heterolytically dissociated on pure CeO_2 surfaces, and H_2O evolution (and Ce^{3+} formation) is limited by the transformation of heterolytic H_2 dissociation products into

https://doi.org/10.1021/jacsau.3c00330
JACS Au 2023, 3, 2299−2313

homolytic products. Pt drives the homolytic dissociation of H_2 and subsequent H-spillover at a much lower temperature compared to heterolytic H_2 dissociation on pure CeO_2 surfaces. The change in the mechanism of H_2 dissociation on the CeO_2 surface caused by Pt results in a >2× larger saturation surface hydroxyl coverage on Pt/CeO_2 compared to pure CeO_2. As a result of Pt promoting H-spillover onto CeO_2 surfaces, the conversion of heterolytic H_2 dissociation products into homolytic products no longer restricts the rate of H_2O evolution on the Pt/CeO_2 surface, and thus, it seems that H_2O evolution is promoted across CeO_2 surfaces, even far away from Pt. In addition, spatially resolved in situ EELS show that Ce^{3+} formed by spillover H preferentially localize at and around the boundary between CeO_2 particles rather than localizing around Pt, suggesting that the H_2O evolution may occur mainly at the CeO_2−CeO_2 boundary. That is, the impact of Pt on surface reactions on CeO_2 is global and not just localized at the Pt−CeO_2 interface. The V_o formation (as a result of H_2O evolution) at the boundary between CeO_2 particles for Pt/CeO_2 is thought to induce surface reconstruction and drive the alignment of neighboring CeO_2 particles to produce boundaries that stabilize the higher concentrations of surface hydroxyls and Ce^{3+} and enable the faster rates of H-spillover. This study provides new insights into the PGM-promoted CeO_2 surface reactions with H_2, which are essential for understanding various catalytic processes, by considering the effect of the spatial heterogeneity of powder catalysts.

■ ASSOCIATED CONTENT

Supporting Information

The Supporting Information is available free of charge at https://pubs.acs.org/doi/10.1021/jacsau.3c00330.

Experimental details, XRD pattern, CO-IR spectra, CO oxidation reactivity data, additional H_2-TPR curves, additional IR spectra collected under H_2, additional STEM imaging and EELS mapping, in situ XANES spectra collected under H_2, summary of DFT studies over H_2 reaction with CeO_2 surfaces, additional discussions on the reactivity of Pt SAs vs NCs, quantitative interpretation of IR, assignment of the IR band at ∼2130 cm^{-1}, EELS data collection, and Ce^{3+} % estimation using EEL spectra, H_2-TPR curves, and FTIR spectra (PDF)

■ AUTHOR INFORMATION

Corresponding Authors

Xiaoqing Pan − *Department of Materials Science and Engineering, University of California Irvine, Irvine, California 92697, United States; Department of Physics and Astronomy and Irvine Materials Research Institute (IMRI), University of California Irvine, Irvine, California 92697, United States;* orcid.org/0000-0002-0965-8568; Email: xiaoqinp@uci.edu

Phillip Christopher − *Department of Chemical Engineering, University of California Santa Barbara, Santa Barbara, California 93106, United States;* orcid.org/0000-0002-4898-5510; Email: pchristopher@ucsb.edu

Authors

Jaeha Lee − *Department of Chemical Engineering, University of California Santa Barbara, Santa Barbara, California 93106, United States*

Peter Tieu − *Department of Chemistry, University of California Irvine, Irvine, California 92697, United States;* orcid.org/0000-0001-8727-2313

Jordan Finzel − *Department of Chemical Engineering, University of California Santa Barbara, Santa Barbara, California 93106, United States;* orcid.org/0000-0002-4758-8740

Wenjie Zang − *Department of Materials Science and Engineering, University of California Irvine, Irvine, California 92697, United States*

Xingxu Yan − *Department of Materials Science and Engineering, University of California Irvine, Irvine, California 92697, United States;* orcid.org/0000-0001-7991-4849

George Graham − *Department of Materials Science and Engineering, University of California Irvine, Irvine, California 92697, United States; Department of Materials Science and Engineering, University of Michigan, Ann Arbor, Michigan 48109, United States*

Complete contact information is available at: https://pubs.acs.org/10.1021/jacsau.3c00330

Author Contributions

#J.L. and P.T. contributed equally to this work.

Notes

The authors declare no competing financial interest.

■ ACKNOWLEDGMENTS

This work was supported by the National Science Foundation (NSF) awards under grant nos. CBET-2031494, CBET-2031512, and CHE-1955786. The authors also acknowledge the use of facilities and instrumentation at the UC Irvine Materials Research Institute (IMRI) supported in part by the NSF through the MRSEC program (DMR-2011967). This work was also supported by a Postdoctoral Fellowship program granted by the National Research Foundation of Korea (NRF) (2020R1A6A3A03039683) (J.L.). J.F. would like to acknowledge support from the National Science Foundation Graduate Research Fellowship Program (NSF GRFP) under grant no. 1650114 and the U.S. Department of Energy, Office of Science, Office of Workforce Development for Teachers and Scientists, and Office of Science Graduate Student Research (SCGSR) program. The SCGSR program is administered by the Oak Ridge Institute for Science and Education for the DOE under contract number DE-SC0014664.

■ REFERENCES

(1) Trovarelli, A. Catalytic properties of ceria and CeO_2-containing materials. *Catal. Rev.* **1996**, *38*, 439−520.

(2) Aireddy, D. R.; Ding, K. Heterolytic Dissociation of H_2 in Heterogeneous Catalysis. *ACS Catal.* **2022**, *12*, 4707−4723.

(3) Xing, F.; Nakaya, Y.; Yasumura, S.; Shimizu, K.-i.; Furukawa, S. Ternary platinum−cobalt−indium nanoalloy on ceria as a highly efficient catalyst for the oxidative dehydrogenation of propane using CO_2. *Nat. Catal.* **2022**, *5*, 55−65.

(4) Zhang, Q.; Bu, J.; Wang, J.; Sun, C.; Zhao, D.; Sheng, G.; Xie, X.; Sun, M.; Yu, L. Highly efficient hydrogenation of nitrobenzene to aniline over Pt/CeO_2 catalysts: The shape effect of the support and key role of additional Ce^{3+} sites. *ACS Catal.* **2020**, *10*, 10350−10363.

(5) Guo, Y.; Mei, S.; Yuan, K.; Wang, D.-J.; Liu, H.-C.; Yan, C.-H.; Zhang, Y.-W. Low-temperature CO_2 methanation over CeO_2-supported Ru single atoms, nanoclusters, and nanoparticles competitively tuned by strong metal−support interactions and H-spillover effect. *ACS Catal.* **2018**, *8*, 6203−6215.
(6) Kalamaras, C. M.; Americanou, S.; Efstathiou, A. M. Redox" vs "associative formate with−OH group regeneration" WGS reaction mechanism on Pt/CeO_2: effect of platinum particle size. *J. Catal.* **2011**, *279*, 287−300.
(7) Vecchietti, J.; Bonivardi, A.; Xu, W.; Stacchiola, D.; Delgado, J. J.; Calatayud, M.; Collins, S. E. Understanding the role of oxygen vacancies in the water gas shift reaction on ceria-supported platinum catalysts. *ACS Catal.* **2014**, *4*, 2088−2096.
(8) Gao, Y.; Li, R.; Chen, S.; Luo, L.; Cao, T.; Huang, W. Morphology-dependent interplay of reduction behaviors, oxygen vacancies and hydroxyl reactivity of CeO_2 nanocrystals. *Phys. Chem. Chem. Phys.* **2015**, *17*, 31862−31871.
(9) Karim, W.; Spreafico, C.; Kleibert, A.; Gobrecht, J.; VandeVondele, J.; Ekinci, Y.; van Bokhoven, J. A. Catalyst support effects on hydrogen spillover. *Nature* **2017**, *541*, 68−71.
(10) Beck, A.; Kazazis, D.; Ekinci, Y.; Li, X.; Müller Gubler, E. A.; Kleibert, A.; Willinger, M.-G.; Artiglia, L.; van Bokhoven, J. A. The Extent of Platinum-Induced Hydrogen Spillover on Cerium Dioxide. *ACS Nano* **2022**, *17*, 1091−1099.
(11) Lykhach, Y.; Staudt, T.; Vorokhta, M.; Skála, T.; Johánek, V.; Prince, K. C.; Matolín, V.; Libuda, J. Hydrogen spillover monitored by resonant photoemission spectroscopy. *J. Catal.* **2012**, *285*, 6−9.
(12) Prins, R. Hydrogen spillover. Facts and fiction. *Chem. Rev.* **2012**, *112*, 2714−2738.
(13) Lin, W.; Herzing, A.; Kiely, C.; Wachs, I. Probing metal−support interactions under oxidizing and reducing conditions: in situ Raman and infrared spectroscopic and scanning transmission electron microscopic− X-ray energy-dispersive spectroscopic investigation of supported platinum catalysts. *J. Phys. Chem. C* **2008**, *112*, 5942−5951.
(14) Ruiz Puigdollers, A.; Schlexer, P.; Tosoni, S.; Pacchioni, G. Increasing oxide reducibility: the role of metal/oxide interfaces in the formation of oxygen vacancies. *ACS Catal.* **2017**, *7*, 6493−6513.
(15) Chen, A.; Yu, X.; Zhou, Y.; Miao, S.; Li, Y.; Kuld, S.; Sehested, J.; Liu, J.; Aoki, T.; Hong, S.; et al. Structure of the catalytically active copper−ceria interfacial perimeter. *Nat. Catal.* **2019**, *2*, 334−341.
(16) Lawrence, E. L.; Crozier, P. A. Oxygen transfer at metal-reducible oxide nanocatalyst interfaces: Contrasting carbon growth from ethane and ethylene. *ACS Appl. Nano Mater.* **2018**, *1*, 1360−1369.
(17) Kropp, T.; Lu, Z.; Li, Z.; Chin, Y.-H. C.; Mavrikakis, M. Anionic single-atom catalysts for CO oxidation: support-independent activity at low temperatures. *ACS Catal.* **2019**, *9*, 1595−1604.
(18) Bliem, R.; van der Hoeven, J.; Zavodny, A.; Gamba, O.; Pavelec, J.; de Jongh, P. E.; Schmid, M.; Diebold, U.; Parkinson, G. S. An Atomic-Scale View of CO and H2 Oxidation on a Pt/Fe_3O_4 Model Catalyst. *Angew. Chem.* **2015**, *127*, 14205−14208.
(19) DeRita, L.; Dai, S.; Lopez-Zepeda, K.; Pham, N.; Graham, G. W.; Pan, X.; Christopher, P. Catalyst architecture for stable single atom dispersion enables site-specific spectroscopic and reactivity measurements of CO adsorbed to Pt atoms, oxidized Pt clusters, and metallic Pt clusters on TiO_2. *J. Am. Chem. Soc.* **2017**, *139*, 14150−14165.
(20) Resasco, J.; DeRita, L.; Dai, S.; Chada, J. P.; Xu, M.; Yan, X.; Finzel, J.; Hanukovich, S.; Hoffman, A. S.; Graham, G. W.; et al. Uniformity is key in defining structure−function relationships for atomically dispersed metal catalysts: The case of Pt/CeO_2. *J. Am. Chem. Soc.* **2019**, *142*, 169−184.
(21) Hoffman, A. S.; Singh, J. A.; Bent, S. F.; Bare, S. R. In situ observation of phase changes of a silica-supported cobalt catalyst for the Fischer−Tropsch process by the development of a synchrotron-compatible in situ/operando powder X-ray diffraction cell. *J. Synchrotron Radiat.* **2018**, *25*, 1673−1682.
(22) Khoobiar, S. Particle to particle migration of hydrogen atoms on platinum-alumina catalysts from particle to neighboring particles. *J. Phys. Chem.* **1964**, *68*, 411−412.
(23) Boaro, M.; Vicario, M.; De Leitenburg, C.; Dolcetti, G.; Trovarelli, A. The use of temperature-programmed and dynamic/transient methods in catalysis: characterization of ceria-based, model three-way catalysts. *Catal. Today* **2003**, *77*, 407−417.
(24) Désaunay, T.; Bonura, G.; Chiodo, V.; Freni, S.; Couzinié, J.-P.; Bourgon, J.; Ringuedé, A.; Labat, F.; Adamo, C.; Cassir, M. Surface-dependent oxidation of H_2 on CeO_2 surfaces. *J. Catal.* **2013**, *297*, 193−201.
(25) Giordano, F.; Trovarelli, A.; de Leitenburg, C.; Giona, M. A model for the temperature-programmed reduction of low and high surface area ceria. *J. Catal.* **2000**, *193*, 273−282.
(26) Maurer, F.; Beck, A.; Jelic, J.; Wang, W.; Mangold, S.; Stehle, M.; Wang, D.; Dolcet, P.; Gänzler, A. M.; Kübel, C.; et al. Surface Noble Metal Concentration on Ceria as a Key Descriptor for Efficient Catalytic CO Oxidation. *ACS Catal.* **2022**, *12*, 2473−2486.
(27) Lee, J.; Ryou, Y.; Kim, J.; Chan, X.; Kim, T. J.; Kim, D. H. Influence of the defect concentration of ceria on the Pt dispersion and the CO oxidation activity of Pt/CeO_2. *J. Phys. Chem. C* **2018**, *122*, 4972−4983.
(28) Finzel, J.; Sanroman Gutierrez, K. M.; Hoffman, A. S.; Resasco, J.; Christopher, P.; Bare, S. R. Limits of Detection for EXAFS Characterization of Heterogeneous Single-Atom Catalysts. *ACS Catal.* **2023**, *13*, 6462−6473.
(29) Beck, A.; Rzepka, P.; Marshall, K. P.; Stoian, D.; Willinger, M. G.; van Bokhoven, J. A. Hydrogen Interaction with Oxide Supports in the Presence and Absence of Platinum. *J. Phys. Chem. C* **2022**, *126*, 17589−17597.
(30) Negreiros, F. R.; Camellone, M. F.; Fabris, S. Effects of thermal fluctuations on the hydroxylation and reduction of ceria surfaces by molecular H_2. *J. Phys. Chem. C* **2015**, *119*, 21567−21573.
(31) Werner, K.; Weng, X.; Calaza, F.; Sterrer, M.; Kropp, T.; Paier, J.; Sauer, J.; Wilde, M.; Fukutani, K.; Shaikhutdinov, S.; et al. Toward an understanding of selective alkyne hydrogenation on ceria: on the impact of O vacancies on H_2 interaction with $CeO_2(111)$. *J. Am. Chem. Soc.* **2017**, *139*, 17608−17616.
(32) Li, Z.; Werner, K.; Qian, K.; You, R.; Płucienik, A.; Jia, A.; Wu, L.; Zhang, L.; Pan, H.; Kuhlenbeck, H.; et al. Oxidation of reduced ceria by incorporation of hydrogen. *Angew. Chem., Int. Ed.* **2019**, *58*, 14686−14693.
(33) Matz, O.; Calatayud, M. Breaking H_2 with CeO_2: effect of surface termination. *ACS Omega* **2018**, *3*, 16063−16073.
(34) Wang, Z.-Q.; Chu, D.-R.; Zhou, H.; Wu, X.-P.; Gong, X.-Q. Role of Low-Coordinated Ce in Hydride Formation and Selective Hydrogenation Reactions on CeO_2 Surfaces. *ACS Catal.* **2021**, *12*, 624−632.
(35) Chen, B.; Ma, Y.; Ding, L.; Xu, L.; Wu, Z.; Yuan, Q.; Huang, W. Reactivity of hydroxyls and water on a $CeO_2(111)$ thin film surface: the role of oxygen vacancy. *J. Phys. Chem. C* **2013**, *117*, 5800−5810.
(36) Li, Z.; Werner, K.; Chen, L.; Jia, A.; Qian, K.; Zhong, J. Q.; You, R.; Wu, L.; Zhang, L.; Pan, H.; et al. Interaction of hydrogen with ceria: hydroxylation, reduction, and hydride formation on the surface and in the bulk. *Chem.—Eur. J.* **2021**, *27*, 5268−5276.
(37) Fronzi, M.; Piccinin, S.; Delley, B.; Traversa, E.; Stampfl, C. Water adsorption on the stoichiometric and reduced $CeO_2(111)$ surface: A first-principles investigation. *Phys. Chem. Chem. Phys.* **2009**, *11*, 9188−9199.
(38) Chen, H. T.; Choi, Y. M.; Liu, M.; Lin, M.-C. A theoretical study of surface reduction mechanisms of $CeO_2(111)$ and (110) by H_2. *ChemPhysChem* **2007**, *8*, 849−855.
(39) Wu, X.-P.; Gong, X.-Q.; Lu, G. Role of oxygen vacancies in the surface evolution of H at CeO_2 (111): a charge modification effect. *Phys. Chem. Chem. Phys.* **2015**, *17*, 3544−3549.
(40) García-Melchor, M.; López, N. Homolytic products from heterolytic paths in H_2 dissociation on metal oxides: the example of CeO_2. *J. Phys. Chem. C* **2014**, *118*, 10921−10926.

https://doi.org/10.1021/jacsau.3c00330
JACS Au 2023, 3, 2299−2313

(41) Fernández-Torre, D.; Carrasco, J.; Ganduglia-Pirovano, M. V.; Pérez, R. Hydrogen activation, diffusion, and clustering on CeO_2 (111): A DFT+ U study. *J. Chem. Phys.* **2014**, *141*, 014703.
(42) Molinari, M.; Parker, S. C.; Sayle, D. C.; Islam, M. S. Water adsorption and its effect on the stability of low index stoichiometric and reduced surfaces of ceria. *J. Phys. Chem. C* **2012**, *116*, 7073−7082.
(43) Vikanova, K.; Redina, E.; Kustov, L. Hydrogen spillover on cerium-based catalysts. *Russ. Chem. Bull.* **2022**, *71*, 1579−1592.
(44) Alayoglu, S.; An, K.; Melaet, G. r. m.; Chen, S.; Bernardi, F.; Wang, L. W.; Lindeman, A. E.; Musselwhite, N.; Guo, J.; Liu, Z.; et al. Pt-mediated reversible reduction and expansion of CeO_2 in Pt nanoparticle/mesoporous CeO_2 catalyst: In situ X-ray spectroscopy and diffraction studies under redox (H_2 and O_2) atmospheres. *J. Phys. Chem. C* **2013**, *117*, 26608−26616.
(45) Mahdavi-Shakib, A.; Kumar, K. B. S.; Whittaker, T. N.; Xie, T.; Grabow, L. C.; Rioux, R. M.; Chandler, B. D. Kinetics of H_2 adsorption at the metal−support interface of Au/TiO_2 catalysts probed by broad background IR absorbance. *Angew. Chem.* **2021**, *133*, 7814−7822.
(46) Binet, C.; Badri, A.; Lavalley, J.-C. A spectroscopic characterization of the reduction of ceria from electronic transitions of intrinsic point defects. *J. Phys. Chem.* **1994**, *98*, 6392−6398.
(47) Wu, W.; Savereide, L. M.; Notestein, J.; Weitz, E. In-situ IR spectroscopy as a probe of oxidation/reduction of Ce in nanostructured CeO_2. *Appl. Surf. Sci.* **2018**, *445*, 548−554.
(48) Binet, C.; Daturi, M.; Lavalley, J.-C. IR study of polycrystalline ceria properties in oxidised and reduced states. *Catal. Today* **1999**, *50*, 207−225.
(49) Bozon-Verduraz, F.; Bensalem, A. IR studies of cerium dioxide: influence of impurities and defects. *J. Chem. Soc., Faraday Trans.* **1994**, *90*, 653−657.
(50) Afrin, S.; Bollini, P. On the Utility of Ce^{3+} Spin− Orbit Transitions in the Interpretation of Rate Data in Ceria Catalysis: Theory, Validation, and Application. *J. Phys. Chem. C* **2022**, *127*, 234−247.
(51) Schweke, D.; Shelly, L.; Ben David, R.; Danon, A.; Kostirya, N.; Hayun, S. Comprehensive study of the ceria−H_2 system: effect of the reaction conditions on the reduction extent and intermediates. *J. Phys. Chem. C* **2020**, *124*, 6180−6187.
(52) Zhang, W.; Pu, M.; Lei, M. Theoretical studies on the stability and reactivity of the metal-doped CeO_2(100) surface: toward H_2 dissociation and oxygen vacancy formation. *Langmuir* **2020**, *36*, 5891−5901.
(53) Zhou, M.; Yang, M.; Yang, X.; Zhao, X.; Sun, L.; Deng, W.; Wang, A.; Li, J.; Zhang, T. On the mechanism of H_2 activation over single-atom catalyst: An understanding of Pt_1/WO_x in the hydrogenolysis reaction. *Chin. J. Catal.* **2020**, *41*, 524−532.
(54) Daelman, N.; Capdevila-Cortada, M.; López, N. Dynamic charge and oxidation state of Pt/CeO_2 single-atom catalysts. *Nat. Mater.* **2019**, *18*, 1215−1221.
(55) Resasco, J.; Yang, F.; Mou, T.; Wang, B.; Christopher, P.; Resasco, D. E. Relationship between atomic scale structure and reactivity of Pt catalysts: hydrodeoxygenation of m-cresol over isolated Pt cations and clusters. *ACS Catal.* **2019**, *10*, 595−603.
(56) Liu, L.; Meira, D. M.; Arenal, R.; Concepcion, P.; Puga, A. V.; Corma, A. Determination of the evolution of heterogeneous single metal atoms and nanoclusters under reaction conditions: which are the working catalytic sites? *ACS Catal.* **2019**, *9*, 10626−10639.
(57) Lykhach, Y.; Figueroba, A.; Camellone, M. F.; Neitzel, A.; Skála, T.; Negreiros, F. R.; Vorokhta, M.; Tsud, N.; Prince, K. C.; Fabris, S.; et al. Reactivity of atomically dispersed Pt^{2+} species towards H_2: model Pt−CeO_2 fuel cell catalyst. *Phys. Chem. Chem. Phys.* **2016**, *18*, 7672−7679.
(58) Fornasiero, P.; Hickey, N.; Kašpar, J.; Montini, T.; Graziani, M. Redox and chemisorptive properties of ex-chloride and ex-nitrate Rh/$Ce_{0.6}Zr_{0.4}O_2$ catalysts: 2. Effect of high-temperature redox cycling. *J. Catal.* **2000**, *189*, 339−348.
(59) Rocchini, E.; Vicario, M.; Llorca, J.; de Leitenburg, C.; Dolcetti, G.; Trovarelli, A. Reduction and oxygen storage behavior of noble metals supported on silica-doped ceria. *J. Catal.* **2002**, *211*, 407−421.
(60) Lin, Y.; Zhou, M.; Tai, X.; Li, H.; Han, X.; Yu, J. Analytical transmission electron microscopy for emerging advanced materials. *Matter* **2021**, *4*, 2309−2339.
(61) Collins, S. M.; Fernandez-Garcia, S.; Calvino, J. J.; Midgley, P. A. Sub-nanometer surface chemistry and orbital hybridization in lanthanum-doped ceria nano-catalysts revealed by 3D electron microscopy. *Sci. Rep.* **2017**, *7*, 5406.
(62) Wang, R.; Crozier, P. A.; Sharma, R.; Adams, J. B. Measuring the redox activity of individual catalytic nanoparticles in cerium-based oxides. *Nano Lett.* **2008**, *8*, 962−967.
(63) Zhang, J.; Huang, F.; Lin, Z. Progress of nanocrystalline growth kinetics based on oriented attachment. *Nanoscale* **2010**, *2*, 18−34.
(64) Nkou Bouala, G.; Clavier, N.; Martin, S.; Léchelle, J.; Favrichon, J.; Brau, H.; Dacheux, N.; Podor, R. From in situ HT-ESEM observations to simulation: how does polycrystallinity affects the sintering of CeO_2 microspheres? *J. Phys. Chem. C* **2016**, *120*, 386−395.
(65) Nkou Bouala, G.; Clavier, N.; Lechelle, J.; Mesbah, A.; Dacheux, N.; Podor, R. In situ HT-ESEM study of crystallites growth within CeO_2 microspheres. *Ceram. Int.* **2015**, *41*, 14703−14711.
(66) Scardi, P.; Leoni, M.; Müller, M.; Di Maggio, R. In situ size-strain analysis of nanocrystalline ceria growth. *Mater. Sci. Eng., A* **2010**, *528*, 77−82.
(67) Watanabe, M.; Seki, T. Initial sintering kinetics of non-stoichiometric CeO_{2-x}. *Mater. Sci. Eng., B* **2021**, *272*, 115369.
(68) Hojo, H.; Mizoguchi, T.; Ohta, H.; Findlay, S. D.; Shibata, N.; Yamamoto, T.; Ikuhara, Y. Atomic structure of a CeO_2 grain boundary: the role of oxygen vacancies. *Nano Lett.* **2010**, *10*, 4668−4672.
(69) Feng, B.; Sugiyama, I.; Hojo, H.; Ohta, H.; Shibata, N.; Ikuhara, Y. Atomic structures and oxygen dynamics of CeO_2 grain boundaries. *Sci. Rep.* **2016**, *6*, 20288.
(70) Lee, J.; Kang, S.; Lee, E.; Kang, M.; Sung, J.; Kim, T. J.; Christopher, P.; Park, J.; Kim, D. H. Aggregation of CeO_2 particles with aligned grains drives sintering of Pt single atoms in Pt/CeO_2 catalysts. *J. Mater. Chem. A* **2022**, *10*, 7029−7035.

https://doi.org/10.1021/jacsau.3c00330
JACS Au 2023, 3, 2299−2313